OXFORD

Journal of Petrology, 2023, **64**, 1–18
https://doi.org/10.1093/petrology/egad069
Advance access publication date 15 September 2023
Original Manuscript

Experimental Constraints on the Ferric Fe Content and Oxygen Fugacity in Subducted Serpentinites

Lisa Eberhard[1,*], Daniel J. Frost[1], Catherine A. McCammon[1], David Dolejš[2] and James A.D. Connolly[3]

[1]Bayerisches Geoinstitut, University of Bayreuth, Universitätsstrasse 30, 95440 Bayreuth, Germany
[2]Institute of Earth and Environmental Sciences, University of Freiburg, Albertstrasse 23b, 79104 Freiburg, Germany
[3]Department of Earth Sciences, Swiss Federal Institute of Technology, Clausiusstrasse 25, 8092 Zürich, Switzerland
*Corresponding author. Department of Earth Sciences, Utrecht University, Vening Meineszgebouw A, Princetonlaan 8a, 3584CB Utrecht, the Netherlands. Tel.: +31302533550; E-Mail: l.eberhard@uu.nl

Abstract

Serpentinites play an important role in the delivery of water into subduction zones. In addition, serpentinites also contain ferric Fe and can transport significant redox potential. We present high-pressure and high-temperature experiments and Mössbauer spectroscopy measurements on natural lizardite and antigorite samples equilibrated at various oxygen fugacities in order to quantify the relationship between the oxygen fugacity $f(O_2)$ and the Fe^{3+}/Fe^{tot} ratio in these two phases. In antigorite, Fe^{3+} partitions into the octahedral site and is charge balanced by tetrahedral Al. In lizardite, tetrahedral Fe^{3+} is observed only at low temperature as well as under high $f(O_2)$, whereas Fe^{3+} prefers the octahedral site at temperatures exceeding 500 °C and at 3 to 5 GPa. Although metastable, lizardite remains in redox equilibrium in our experiments at conditions above the lizardite to antigorite phase transformation at 300 °C and demonstrates a similar stability to antigorite. The Al concentration of lizardite is found to be temperature dependent, and it was possible to reequilibrate the Fe^{3+}/Fe^{tot} ratio of lizardite from 0.1 to 0.9 by using redox buffers such as Fe metal, graphite, graphite–calcite, Re–ReO_2 and Ru–RuO_2. Our experiments on antigorite demonstrate that antigorite does not adjust its Al concentration on experimental time scales. Since Fe^{3+} is charge balanced by Al, it was also not possible to manipulate the Fe^{3+}/Fe^{tot} ratio of antigorite. The coexisting phases, however, show chemical equilibration with this antigorite composition. We have retrieved the standard Gibbs energy for Fe^{3+}- and Al-endmembers of antigorite and lizardite and calculated the metamorphic evolution of subducting serpentinites. The lizardite to antigorite transformation does not cause a decrease in the bulk Fe^{3+}/Fe^{tot} ratio under $f(O_2)$ buffered conditions, in contrast to observations from some natural settings, but does result in the formation of additional magnetite due to antigorite having a lower Fe^{3+}/Fe^{tot} ratio than lizardite at equilibrium. If the $f(O_2)$ of antigorite serpentinite is buffered during subduction, such as due to the presence of graphite and carbonate, the bulk Fe^{3+}/Fe^{tot} ratio decreases progressively. On the other hand, in a closed system where the bulk serpentinite Fe^{3+}/Fe^{tot} ratio remains constant, the $f(O_2)$ increases during subduction. In this scenario, the $f(O_2)$ of an antigorite serpentinite with a typical Fe^{3+}/Fe^{tot} ratio of 0.4 increases from the fayalite–magnetite–quartz to the hematite–magnetite $f(O_2)$ buffer during dehydration. These $f(O_2)$ results confirm earlier inferences that fluids produced by antigorite dehydration may not contain sufficient oxidised sulphur species to oxidise the mantle wedge. Sufficiently high levels of $f(O_2)$ to mobilise oxidised sulphur species may be reached upon antigorite dehydration, however, if closed system behaviour maintains a high bulk redox potential across the lizardite to antigorite phase transformation. Alternatively, oxidation of the mantle wedge might be achieved by oxidising agents from sources in subducted oceanic crust and sediments.

Key words: serpentine; subduction zone; redox; oxygen fugacity; Mössbauer spectroscopy

INTRODUCTION

The key role played by serpentinites in the transport and release of water in subduction zones has been widely recognised (Peacock, 1990; Ulmer & Trommsdorff, 1995; Rüpke *et al.*, 2004; Alt *et al.*, 2012; Spandler & Pirard, 2013; Cannaò *et al.*, 2016; Scambelluri *et al.*, 2019). Serpentinites, formed at slow spreading ridges and within faults in the outer rise domains (Hatakeyama *et al.*, 2017; Arnulf *et al.*, 2022), generally have a distinct alteration mineralogy of lizardite + magnetite ± brucite (±relict olivine and/or pyroxene), which has resulted from the simplified hydration reactions:

$$\text{olivine} + \text{water} \rightarrow \text{lizardite} + \text{brucite} + \text{magnetite} + H_2 \quad (1)$$

$$\text{pyroxene} + \text{brucite} + \text{water} \rightarrow \text{lizardite} + \text{magnetite} + H_2. \quad (2)$$

Eqs. (1) and (2) are redox reactions, and they indicate that in addition to hydration, serpentinisation also raises the oxygen content and redox budget of the lithosphere through the formation of Fe^{3+}-bearing minerals. Although the formation of magnetite during serpentinisation is a complex process whose extent varies significantly among tectonic settings and protolith composition (Frost & Beard, 2007; Klein *et al.*, 2014; Evans *et al.*, 2017), magnetite is almost invariably present in serpentinites. Evans (2008) showed that the bulk rock Fe^{3+}/Fe^{tot} ratio of serpentinised rocks increases with the degree of hydration and ranges from zero to almost unity in completely serpentinised peridotites. Such high bulk rock Fe^{3+}/Fe^{tot} ratios in serpentinites require hematite as the stable Fe-oxide and can only be explained if the serpentine minerals themselves also contain a ferric Fe component.

Received: April 20, 2023. **Revised:** September 8, 2023. **Accepted:** September 13, 2023

Natural lizardite, the stable serpentine mineral at low pressure (Evans, 2004; Schwartz *et al.*, 2013), shows a wide range of composition, with variable Al concentration and Fe^{3+}/Fe^{tot} ratio (Mellini, 1982; Mellini & Zanazzi, 1987; Brigatti *et al.*, 1997; Evans *et al.*, 2012; Mayhew & Ellison, 2020). The trivalent cations are typically charge balanced via Tschermak substitution such as in cronstedtite $Mg_2Fe^{3+}{}_2SiO_5(OH)_4$. Alternatively, Fe^{3+} can be incorporated by the formation of octahedral vacancies as in greenalite $(Fe^{2+},Fe^{3+})_{2\text{-}3}Si_2O_5(OH)_4$ (Evans, 2008; Evans *et al.*, 2012). During serpentinite subduction, lizardite transforms to antigorite, which is generally found to have lower Fe^{3+}/Fe^{tot} ratios and a lower Al concentration than lizardite (Evans *et al.*, 2012; Schwartz *et al.*, 2013; Debret *et al.*, 2014; Mayhew & Ellison, 2020). The stability field of antigorite has been extensively investigated both in the field and by experiments (Ulmer & Trommsdorff, 1995; Wunder & Schreyer, 1997; Bromiley & Pawley, 2003; Padrón-Navarta *et al.*, 2011, 2013; Flemetakis *et al.*, 2022). The substitution of both Fe^{2+} and Al is known to affect the antigorite stability. While Fe^{2+} decreases the stability of antigorite (Merkulova *et al.*, 2016), Al is considered to cause its stability field to expand to higher temperatures (Bromiley & Pawley, 2003; Padrón-Navarta *et al.*, 2013). However, the effect of Fe^{3+} substitution on the stability of various serpentine minerals has not been examined systematically.

Debret *et al.* (2014, 2015) found evidence for a decrease in the bulk Fe^{3+}/Fe^{tot} ratio of natural serpentinites during progressive subduction and linked this reduction to the release of a fluid containing oxidised sulphur species. Such oxidising fluids were suggested to cause the generally more oxidised nature of arc magmas (Parkinson & Arculus, 1999; Kelley & Cottrell, 2009). However, the oxygen fugacity, $f(O_2)$, required to stabilise aqueous sulphate is close to or above the hematite-magnetite buffer, conditions that are not reached by most subducted serpentinites (Evans & Powell, 2015; Piccoli *et al.*, 2019; Evans & Frost, 2021). Using high-pressure and high-temperature experiments, Merkulova *et al.* (2017) found that sulphur release does not necessarily mean sulphate formation. The authors showed a reduction of Fe^{3+} in serpentinites with increasing temperature under $f(O_2)$ conditions likely controlled by the experimental assembly, but argued that the total amount of sulphur and carbon available in natural serpentinites is not sufficient to account for the complete Fe reduction. Instead, large-scale interaction between variably oxidised adjacent lithologies was proposed to facilitate the serpentine reduction.

One potential problem in modelling the redox budget and $f(O_2)$ of serpentinites is the assumption that Fe^{3+} is hosted in magnetite only, while ignoring the Fe^{3+} substitution in serpentine. The consequences of such substitution for the $f(O_2)$ and the stability of magnetite and other redox-sensitive minerals such as carbonates and sulphides have been examined by preliminary thermodynamic calculations that rely on estimates of Fe^{3+}-serpentine thermodynamic properties (Evans & Powell, 2015). These calculations are crucial to constrain the oxidising capacity of subducted serpentinites and the capacity of the released fluids to transport the redox budget into the mantle wedge (Evans & Frost, 2021). However, to date, there exist no experimental data to assess these estimates.

Here we examine the influence of Fe^{3+} on the stability of lizardite and antigorite using high-pressure and high-temperature experiments performed on natural serpentinite starting materials under constrained $f(O_2)$. The Fe^{3+} concentrations of serpentine were measured using Mössbauer spectroscopy. The relationship between the serpentine Fe^{3+} concentrations and the $f(O_2)$ was used to determine the standard Gibbs energies for Fe^{3+}- and Al-endmembers of antigorite and lizardite. Furthermore, we explore the phase equilibria of serpentinites during progressive subduction and examine the relationship between the bulk rock composition, in particular, the Al_2O_3 concentration and the Fe^{3+}/Fe^{tot} ratio, and the $f(O_2)$ of the subducting lithospheric slab. Finally, we discuss the consequences for the redox state of fluids generated by serpentinite dehydration reactions.

METHODS

Starting materials

Previous attempts to synthesise serpentine minerals have documented very limited growth within reasonable experimental timescales (Wunder *et al.*, 1997, 2001; McCollom *et al.*, 2020a, 2020b). Consequently, we selected two natural starting materials for the experiments: antigorite serpentinite and lizardite serpentinite. The two samples differ in their mineralogical and chemical composition but were chosen due to their significantly different bulk Fe^{3+}/Fe^{tot} ratios. The antigorite serpentinite (sample Zer_1701) from the Zermatt ophiolite (Li *et al.*, 2004) contains antigorite (>95%), magnetite (<5%) and minor Fe sulphides. Few grains of diopside, magnesite and Ti-clinohumite were determined by optical microscopy. Antigorite was confirmed by Raman spectroscopy (supporting information B1). The lizardite serpentinite (sample Lig_1602) from Val Graveglia, in the Internal Liguride units of the Northern Apennines (Principi *et al.*, 2004), is a massive serpentinite containing >95% lizardite, <5% opaque phases and minor amounts of chlorite. Raman spectroscopy (supporting information B1) confirmed lizardite, in agreement with the weak metamorphic overprint of these rocks. Three microscopically distinct types of lizardite are present in the sample. The first type (lizardite I) is yellowish pleochroic. The second type (lizardite II) is colourless and has replaced minerals with a pronounced cleavage, probably pyroxene. Some of the lizardite I and II grains are overgrown by light green-brown grains, identified as chlorite based on its anomalous brownish interference colour. The youngest generation of lizardite (lizardite III) grew in cross-cutting veins and has undulous extinction. These veins often contain angular magnetite grains. Magnetite is also observed as anhedral grains with a grain size ranging from 0.01 to 1 mm enclosed in lizardite I and II. An additional minor opaque phase is anhedral pyrite with pale yellowish colour in reflected light. A few late crosscutting veins filled with high interference minerals (not further analysed) were also observed.

High-pressure experiments

The serpentine samples were pulverised to grain sizes of 10–30 μm. The first two experiments (V1048, V1056) were run with the pure antigorite serpentinite powder. In all other experiments, the powder was mixed either with iridium metal, serving as redox sensor, or with a redox buffer, including Fe metal, graphite, graphite + calcite, Re + ReO_2 and Ru + RuO_2. All added chemicals were reagent-grade powders. The proportions added to obtain the starting mixes are given in Table 1.

The experiments were conducted in a Walker-type multi-anvil press at the Bayerisches Geoinstitut (BGI) with standard 18/11 BGI assemblies (Keppler & Frost, 2005). The pressure was calibrated using the quartz–coesite transition. The temperature was deduced from power–temperature correlations and calibrated against a type D thermocouple, which was included in each experiment. Errors are conservatively estimated to be 20 °C and 0.2 GPa. The starting materials were loaded in gold capsules and

Table 1: Mass fraction of Ir metal and/or redox buffers added to the serpentinite starting material. The name of the buffer corresponds to the abbreviation used in Table 2

Name	Composition
Ir	5 wt. % Ir
Ir, C	4 wt. % Ir + 10 wt. % graphite
RRU	2 wt. % Ru + 8 wt. % RuO_2
RRE	2 wt. % Re + 8 wt. % ReO_2
CbC	2 wt. % graphite +8 wt. % calcite
Fe	10 wt. % Fe metal

welded shut. Experimental conditions were 469–926 °C and 2.5–5 GPa, with run times varying between 2 and 8 days. Capsules were pierced after the experiments to confirm that any released fluid remained in the capsule. Experimental run conditions are summarised in Table 2.

The recovered capsules were cut in half. One capsule half was mounted in epoxy and polished for optical and chemical analyses. The other half was polished on both sides for Mössbauer spectroscopy.

Analytical methods

Phase identification

A Zeiss LEO 1530 scanning electron microscope (SEM) equipped with an energy-dispersive X-ray detector operating with 20 kV acceleration voltage was used for semi-quantitative phase identification in the experimental products. The major element composition of the minerals in the starting materials and the experimental products was determined with a JEOL JX8200 microprobe operating with 15 kV acceleration voltage. All samples were coated with a 10 nm thick carbon layer. The beam current and diameter were optimised for each phase: 20 nA and a focused beam for olivine, pyroxene, garnet, oxides and metals; 10–15 nA and a 2–5 μm beam diameter for serpentine, chlorite and carbonates. Volatile contents of hydrous minerals and carbonates were estimated by difference from the oxide total. In some experiments, the grain size of olivine and pyroxene was less than 0.5 μm, and the bulk composition of olivine + pyroxene aggregates was measured. In this case, we used concentration trends to extrapolate the compositions of each contributing phase or estimated the phase composition from experiments performed at similar conditions. Mean mineral compositions and the corresponding standard deviations (2% if only one grain could be measured) are reported in Tables A-1 to A-9. In order to distinguish serpentine polymorphs in the starting materials and the experimental products, a WiTec ALPHA300 R confocal microscope at Utrecht University, equipped with a 532-nm laser, 50× objective lens and a spectral grating of 1800 grooves/cm, was used. Data acquisition and processing were performed with the software WiTec ProjectFive. All spectra can be found in the supporting information B-1.

Determination of phase proportions

The proportions of phases in the experimental products are crucial to deconvolute the Mössbauer spectra. We used mass balance calculations to assess the mass fractions of individual minerals in the experimental products. The mass balance was based on the major oxide components SiO_2, Al_2O_3, Cr_2O_3, FeO, MgO, IrO_2 and H_2O. In carbonate-bearing experiments, CaO and CO_2 were used as additional components. We assumed the fluid to be pure H_2O without dissolved aqueous species. For carbonate-bearing experiments, a small fraction of dissolved carbon-bearing species CO_3^{2-} might be expected in the fluid (Caciagli & Manning, 2003; Manning, 2013), but it cannot be reliably estimated by mass balance. For each component i, the equation $i_{bulk} + d = \Sigma m_j(i_j)$ is written. The set of equations for each experimental run is solved for the mass fraction m of each mineral j by minimising the residual d. The bulk composition of each experimental run was calculated from the starting mixture (Table 1), whereby the magnetite content in the serpentinite powder (obtained from Mössbauer spectroscopy) is as follows: 2 wt. % magnetite in the antigorite serpentinite and 3 wt. % magnetite in the lizardite serpentinite. To estimate the uncertainties arising from compositional variations, we used a Monte Carlo approach with 1000 minimisation steps per experimental run. For each step, both i_{bulk} and i_j were varied within the measured standard deviation. The mass fractions of minerals in the run products are reported in Table A-10.

Oxygen fugacity calculation

In redox buffered experiments, the oxygen fugacity is determined by the equilibrium:

$$\text{metal} + O_2 = \text{metal oxide}. \quad (3)$$

The oxygen fugacity in unbuffered experiments has been calculated from several mineral equilibria involving magnetite or hematite and, in some cases, employing iridium–iron alloy (Ir,Fe) as a sliding redox sensor (Woodland & O'Neill, 1997; Stagno *et al.*, 2015). Representative equilibria are as follows:

$$3\ \text{Fe (alloy)} + 2\ O_2 = \text{Mag} \quad (4)$$

$$3\ \text{Fa} + O_2 = 2\ \text{Mag} + 3\ \text{Qz (FMQ)} \quad (5)$$

$$2\ \text{Fs} + O_2 = 2\ \text{Hem} + 4\ \text{Qz}, \quad (6)$$

where mineral abbreviations are according to Whitney & Evans (2010). A detailed list of all equilibria used to determine oxygen fugacities as well as thermodynamic data and activity–composition relations are provided in the supporting information B-2.

Ferric iron analysis

We used Mössbauer spectroscopy to examine the distribution and redox state of Fe in the starting materials and experimental products. The starting materials were analysed as powders with a conventional ^{57}Co Mössbauer source (effective diameter of 5 mm). Approximately 200 mg of powder was loaded into a 12-mm diameter plastic sample holder. The experimental products were measured as ~500 μm thick sections with a ^{57}Co point source (effective diameter of 0.5 mm). The ideal thickness of the samples was calculated using absorption coefficients. The spectra were collected with a constant acceleration profile over the velocity range of −5 to 5 and/or −12 to 12 mm/s. Experiments with a significant hematite fraction were measured over the velocity range of −4 to 4 mm/s in order to increase the resolution on the silicate fraction. The velocity scale was calibrated with a 25 μm thick α-Fe foil. Fitting of the spectra was performed with the Matlab code MossA and a full transmission integral was applied (Prescher *et al.*, 2012). Spectra were fit with a Pseudo-Voigt line shape for silicates to account for the next-nearest-neighbour effects, whereas a Lorentzian line shape was used for oxides. The magnetic sextet was fit on the ±12 mm/s spectra and fixed to these values in the ±5 mm/s spectra. In the ±4 mm/s

Table 2: Experimental run conditions and assemblages

Name	T (°C)	P (GPa)	Time (h)	Starting mixture	Log $f(O_2)$	ΔFMQ	Srp	Chl	Grt	Ol	Px	Mag	Hem	Cb	Minor phases
Zer_1701 starting material—unbuffered															
V1087	469	3	72	Ir	−19.6(1)	1.79	x					x			
V1090	572	4	62	Ir	−15.7(1)	0.69	x					x			(ps)(Mgs)
V1159b	572	5	98	Ir	−14.5(1)	0.83	x					x			
V1104	580	3	86	Ir	−15.8(2)	1.48	x					x			(ps)(Mgs)
V1105	627	3	86	Ir	−14.5(4)	1.41	x	x		x	x*	x			
V1111	644	3	62	Ir	−16.6(13)	−0.12	x	x		x	x**	(x)			
V1092	696	3.5	96	Ir	−12.3(4)	1.43		x		x*	x*	x			
V1102	780	3	68	Ir	−12.6(20)	−0.26			x	x	x*	(x)			
V1048	924	2.5	48	Pure	–	–				x	x				
V1056	926	2.5	72	Pure	–	–				x	x				Spl
Lig_1602 starting material—unbuffered															
V1125	483	3	80	Ir	−19.5(1)	1.33	x					x			(ps)
V1114	526	3	98	Ir	−18.0(4)	1.16	x	x		x		(x)			
V1159a	572	5	98	Ir	−14.6(6)	0.75	x			x		(x)			
V1116	595	3	192	Ir	−15.3(1)	1.62	x	x		x	x**	x			
V1117	609	3	48	Ir	−14.8(2)	1.69	x	x		x	x**	x			
V1113	607	3	87	Ir	−15.2(2)	1.32		x		x	x	x			Mgs
V1115	648	3	110	Ir	−14.1(5)	1.25		x		x	x*	x			
Zer_1701 starting material—buffered															
V1143a	494	3	90	RRU	n.e.	n.e.	x					x			(Mgs)
V1160b	526	3	99	RRU	n.e.	n.e.	x					x			
V1148a	487	3	97	CbC	−22.67[3]	−2.57	x				x	x		Arg	Gr
V1153b	526	5	98	CbC	−20.70[3]	−2.89	x			x**	x	x		Mgs	Gr
Lig_1602 starting material—buffered															
V1132a	481	3	96	RRU	−10.03[1]	10.82	x						x		
V1146a	528	5	96	RRU	−7.56[1]	9.27	x	x					x		
V1150a	580	5	92	RRU	−6.54[1]	8.67	x			x			x		Mgs
V1127	640	3	81	RRU	−6.73[1]	8.84	x	x		x	x		x		Mgs
V1135a	685	3	93	RRU	−6.00[1]	8.42		x		x	x		x		Mgs
V1138a	782	3	117	RRU	−4.63[1]	7.64				x	x		x		(Mgs)
V1132b	481	3	96	RRE	−19.04[2]	1.83	x	x		(x)		x			
V1146b	528	5	96	RRE	−16.11[2]	0.72	x			(x)		x			Spl/ (ps)
V1150b	580	5	92	RRE	−14.53[2]	0.68	x			x		x			
V1128	631	3	84	RRE	−14.27[2]	1.54	x	x		x	x	x			Mgs
V1135b	685	3	93	RRE	−12.93[2]	1.48		x		x	x	x			
V1138b	782	3	117	RRE	−10.86[2]	1.41				x	x	(x)			Mgs/ Spl
V1148b	487	3	97	CbC	−22.30[3]	−2.19	x			x**	x**	x		Mgs	Gr
V1153a	526	5	98	CbC	−20.70[3]	−2.89	x			x**	x**	(x)		Mgs	Gr
V1143b	494	3	90	Ir, C	−18.5(1)	1.62	x			x		(x)			Gr
V1139	498	3	63	Fe	−26.38[4]	−6.20	x			x					Fe/FeO/(Fa)
V1140	592	3	94	Fe	−22.68[4]	−5.74		x		x					Fe/Fa

Starting mixture refers to compositions given in Table 1. $f(O_2)$ is calculated based on various phase equilibria (see supporting information B-2) or from buffer equilibria given as [1]$Ru + O_2 = RuO_2$; [2]$Re + O_2 = ReO_2$; [3]carbonate–silicate equilibria (Eberhard *et al.*, 2023), [4]$Fe + 0.5O_2 = FeO$. n.e. = not equilibrated. Mineral abbreviations are after Whitney & Evans (2010); ps = secondary phases. Minerals in parentheses were observed with SEM but were too small to be measured on the microprobe. * indicates extrapolated phase composition (see Methods section for more information). ** indicates composition estimated from experiments at similar conditions. Full mineral analyses can be found in supporting information A.

spectra, the magnetic fraction was fit with two doublets having identical centre shifts. Variable area ratios for both doublets and sextets were enabled to account for preferred orientation in the sample. Hyperfine parameters are listed in Tables A-11 to A-13. All spectra and additional information on the treatment of overlapping absorption bands are given in supporting information B-4 and B-5.

Thermodynamic modelling with Perple_X

Phase diagram calculations were performed by Gibbs energy minimisation with the Perple_X package (Connolly, 2005). We used version 6.9.1 with the database of Holland & Powell (2011), version DS622, and the modified Tait equation of state for solids. The H_2O and H_2 fluid were modelled with the equation of state by Pitzer & Sterner (1994). The following solid solution models were included in the phase equilibrium calculations: olivine—*O(JH)*, orthopyroxene—*Opx(JH)*, garnet—*Grt(JH)* and spinel—*Sp(JH)* from Jennings & Holland (2015); orthoamphibole—*oAmph(DP)* from Diener *et al.* (2007); chlorite—*Chl(W)* from White *et al.* (2014); fluid—*COH Fluid*; brucite—*B*, talc—*T* and clinohumite—*Chum* as ideal solutions. The free energy of the ferric chlorite endmember was adjusted according to Evans & Frost (2021) to obtain a Fe^{3+}/Fe^{tot} ratio for

chlorite that matches literature data. For the lizardite and antigorite solid solutions, we developed new solution models including the Mg-, Fe^{2+}-, Fe^{3+}- and Al-endmembers (see Section 'A new thermodynamic model for ferric Fe serpentine' for more details). Two different bulk compositions were used, corresponding to our two serpentinites used for experiments in this study, i.e., 97 wt. % lizardite + 3 wt. % magnetite, and 98 wt. % antigorite + 2 wt. % magnetite. Additional information and comparison between various models are given in supporting information B-3, and all input files are available in supporting information B-6.

RESULTS

Phase relations

Table 2 summarises mineral assemblages in the experimental products and the $f(O_2)$ determined for each experiment (see supporting information B-2 for additional information). In agreement with previously published phase relations (Padrón-Navarta *et al.*, 2010; Merkulova *et al.*, 2016; Maurice *et al.*, 2020; Flemetakis *et al.*, 2022), the experiments show a stepwise fluid release, between approximately 550 and 780 °C, through the dehydration of serpentine (the term serpentine is used hereafter collectively for both antigorite and lizardite) and chlorite. Prior to dehydration, the stable assemblage is serpentine + magnetite (Fig. 1a). Raman measurements indicate that lizardite did not transform to antigorite and instead persists in a metastable state to temperatures far above the phase transformation expected at approximately 300 °C (Schwartz *et al.*, 2013). The onset of serpentine dehydration is marked by the formation of fine-grained Fe-rich silicates (<1 μm) along the grain boundaries of serpentine and oxides (Fig. 1b). With increasing temperature, the newly formed silicates eventually grow and form patches of olivine and needle-like orthopyroxene with a grain size of up to 10 μm, with interstitial chlorite (Fig. 1c). Although various studies reported an intermediate talc-like phase at the onset of serpentine dehydration (Perrillat *et al.*, 2005; Chollet *et al.*, 2011; Plümper *et al.*, 2017), we could not identify this phase. Magnetite disappears from the assemblages prior to the dehydration of chlorite at temperatures above 700 °C in unbuffered experiments, leaving only small Cr-rich spinel grains (Fig. 1d). At temperatures above chlorite dehydration, the stable assemblage is olivine + orthopyroxene ± spinel below 2.5 GPa, whereas garnet is observed at pressures above 2.5 GPa. Garnet grains are generally >50 μm in diameter and have a poikiloblastic appearance (Fig. 1e).

The phase relations in the redox-buffered experiments are similar to the unbuffered experiments, with the changes in $f(O_2)$ mainly affecting the oxide phases (Table 2). In the redox-buffered experiments, SEM analyses confirmed that all buffer components (metals and oxides) remained dispersed throughout the sample. Only in the two Ru + RuO_2 buffered antigorite-bearing experiments (V1143a, V1160b) the oxide was not observed and was likely exhausted, whereas magnetite has remained stable in both experiments. Consequently, the redox state of these experiments was buffered by the antigorite + magnetite coexistence rather than by the Ru + RuO_2 buffer. In a lizardite-bearing experiment performed at similar conditions (V1132a), hematite was observed.

In experiments where Fe metal or calcite + graphite was added to moderate the $f(O_2)$, chemical reactions occurred between serpentine and the redox buffer. Fe metal was added to two experiments (V1139, V1140) in which wüstite formed around the metal flakes and the iron concentration in silicates close to the metal grains increased (Fig. 1f). In experiments buffered with calcite + graphite, the carbonate reacted with the silicates and formed magnesite and clinopyroxene. Only in one experiment, performed with the antigorite starting material (V1148a), aragonite, confirmed by Raman spectroscopy, remained stable together with minor amounts of clinopyroxene, whereas in an experiment with a lizardite starting material (V1148b) performed under similar conditions magnesite was observed.

Fig. 2 shows the phase relations upon serpentine dehydration, as a function of temperature. The unbuffered experiments indicate that lizardite starts to dehydrate at 500 °C, whereas the same reaction for antigorite is initiated at 600 °C (Fig. 2a, c). Slightly higher dehydration temperatures of 550 °C were observed in lizardite experiments buffered to high $f(O_2)$ (Fig. 2b, d), whereas experiments buffered with graphite or Fe metal have undergone significant dehydration by 500 °C and may even commence dehydration below 450 °C. This behaviour can be described as redox dehydration.

Mineral compositions and element partitioning

Al concentration in serpentine and chlorite

The chemical composition of serpentine, determined by electron microprobe, was recalculated to the sum of 5 cations per formula unit (pfu) for lizardite and to 4.824 cations pfu for antigorite, which corresponds to an $m = 17$ polysome with two tetrahedral sites (Mellini *et al.*, 1987). The Al concentration of antigorite in the experimental products has remained essentially constant, in the range of 0.13 to 0.15 Al pfu. This range is inherited from the starting material and is quite typical for serpentine in ultramafic rocks (Padrón-Navarta *et al.*, 2013; Fig. 3a). Previous experimental studies (Padrón-Navarta *et al.*, 2010; Merkulova *et al.*, 2016; Flemetakis *et al.*, 2022) have also reported antigorite Al concentrations that have remained constant and are independent of the experimental temperature. By contrast, Schwartz *et al.* (2013) reported a positive temperature dependency of Al concentration in natural antigorite from the medium- to high-temperature domains of the *Schistes lustrées*, having equilibration temperatures between 350 and 500 °C at 1.2 GPa.

Lizardite, on the other hand, shows a strongly temperature-dependent Al concentration in the experimental products. The concentration increased from 0.09(7) Al pfu at 480 °C to 0.30(6) Al pfu at 640 °C at 3 to 5 GPa (Fig. 3a). The lizardite Al concentration appears to be only a function of temperature, and it shows no apparent correlation with pressure or $f(O_2)$. More importantly, the Al concentration in lizardite follows a similar temperature trend as observed in natural antigorite (Schwartz *et al.*, 2013), which is displaced to higher absolute values close to the dehydration temperature (Fig. 3a).

The total trivalent cation content in both serpentine phases is inversely correlated with Si (Fig. 3b) due to Tschermak substitution (cf. Padrón-Navarta *et al.*, 2013). Partitioning of Al to chlorite as lizardite dehydrates causes the Al concentration in coexisting chlorite to increase from 1.4(1) Al pfu at 450 °C to 1.8(1) Al pfu at 800 °C. At temperatures exceeding the dehydration of chlorite, Al is incorporated in spinel and/or enstatite below 2.5 GPa or garnet at higher pressures. The Al concentration in orthopyroxene is, in addition, positively correlated with temperature and exceeds 0.2 Al pfu at 650 °C and 2.5 GPa.

Fe^{2+}–Mg partitioning between silicates

Antigorite in the experimental products has a Fe# (molar FeO/[MgO + FeO]) between 0.04 and 0.06 with a weak positive temperature dependency, although these values are comparable to that of the starting material (Fe# = 0.05). The Fe# of lizardite in unbuffered experiments ranges from 0.05 to 0.07 and increases

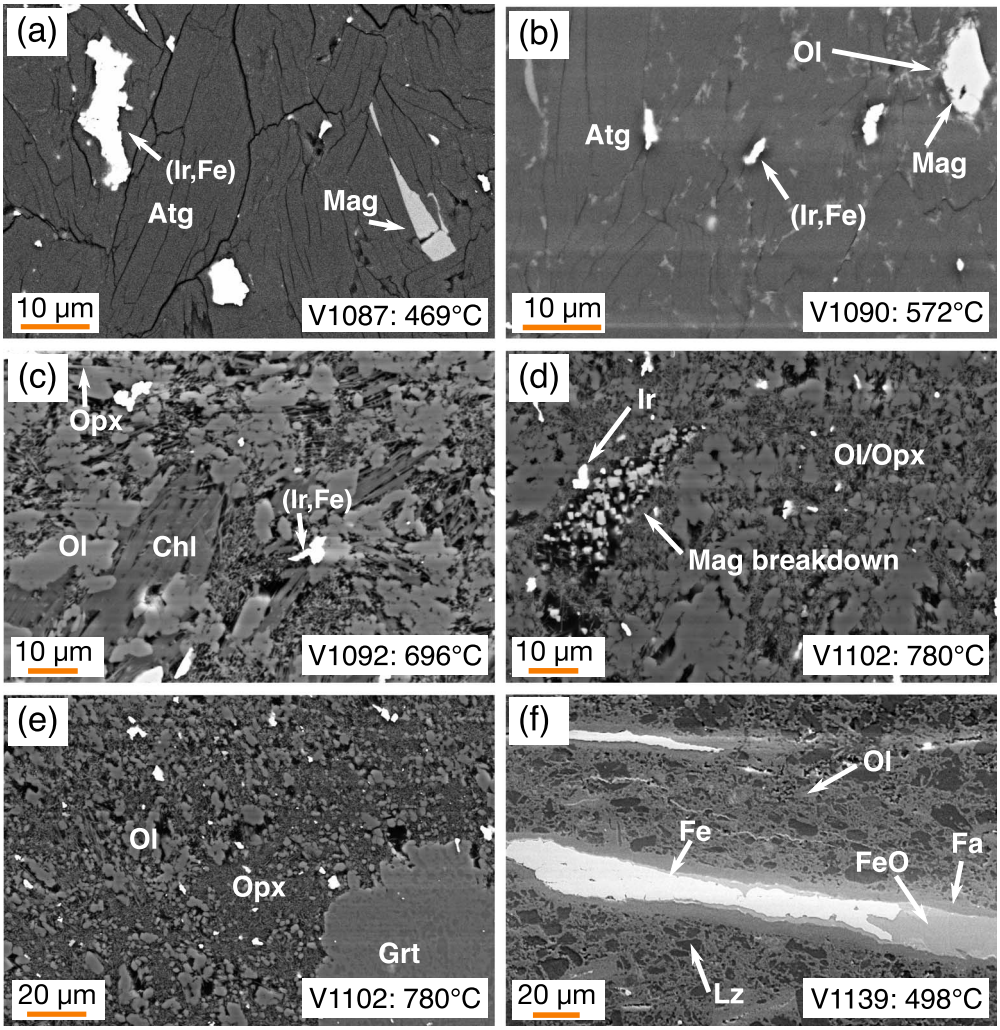

Fig. 1. (a) Experiment V1087 showing a dense antigorite matrix with magnetite and (Ir,Fe) redox sensor. (b) Experiment V1090 showing the formation of Fe-rich silicates along the grain boundaries. (c) Experiment V1092 showing chlorite as the stable intermediate-temperature hydrous mineral. (d) Experiment V1102 showing breakdown of magnetite that leaves behind bright oxide grains. (e) Experiment V1102 showing garnet at temperatures above the final dehydration of chlorite. (f) Experiment V1139 showing Fe metal surrounded by a layer of FeO and fayalitic olivine, which differs in composition from olivine within the matrix.

with temperature, whereas in the redox-buffered experiments, the Fe# strongly depends on the $f(O_2)$ and decreases to near 0 in $Ru + RuO_2$ buffered experiments.

The Fe^{2+}–Mg partitioning between serpentine, olivine, orthopyroxene and chlorite is shown in Fig. 4a, b. The Fe# of olivine follows the trend for metamorphic antigorite–olivine pairs reported by Evans *et al.* (2012). However, the lizardite-bearing experiments with graphite or Fe metal, i.e., under low $f(O_2)$, fall off this trend (V1139 and V1143b). In both of these experiments, the silicate Fe concentration has increased due to oxidation of Fe metal (V1139) or reduction of magnetite (V1143b). The formation of Fe-rich olivine (Fe# = 0.43) in the vicinity of Fe metal flakes was likely faster than the time required for the Fe concentration in lizardite to reach equilibrium. Similar consequences for Fe^{2+}–Mg equilibration between olivine and lizardite might result from magnetite reduction in V1143b. Due to the lack of equilibrium, we will not use these two experiments in the calculations below.

The Fe# in chlorite is around 0.05, and it decreases slightly with increasing $f(O_2)$. The Fe^{2+}–Mg partitioning between olivine and orthopyroxene agrees with the relatively temperature-independent partitioning reported by von Seckendorff *et al.* (1993) and indicates a satisfactory approach to equilibrium, even at temperatures below 600 °C (Fig. 4b).

Iron oxidation state

The Fe^{3+}/Fe^{tot} ratio in the experimental run products was analysed using Mössbauer spectroscopy. The antigorite serpentinite starting material is composed of antigorite and magnetite (Fig. 5a), with antigorite containing ferrous and ferric Fe in the octahedral site with a Fe^{3+}/Fe^{tot} ratio of 0.28(1). Fig. 5b–d illustrates variations in the redox state and Fe^{2+}–Mg partitioning in the antigorite-bearing samples as a function of temperature. The Mössbauer spectrum of an antigorite experiment equilibrated at temperatures below the antigorite dehydration (600 °C) shows the presence of antigorite and magnetite (Fig. 5b), whereas at higher temperatures, the magnetite sextets disappear. Furthermore, while the hydrous minerals, capable of containing Fe^{3+}, dehydrate, Fe^{2+}-bearing olivine and orthopyroxene form and a decrease in the bulk silicate Fe^{3+}/Fe^{tot} ratio is observed (Fig. 5d). Due to the strong overlap of absorption peaks of several phases, determination of the serpentine Fe^{3+}/Fe^{tot} ratio requires additional mass balance constraints (supporting information B-4).

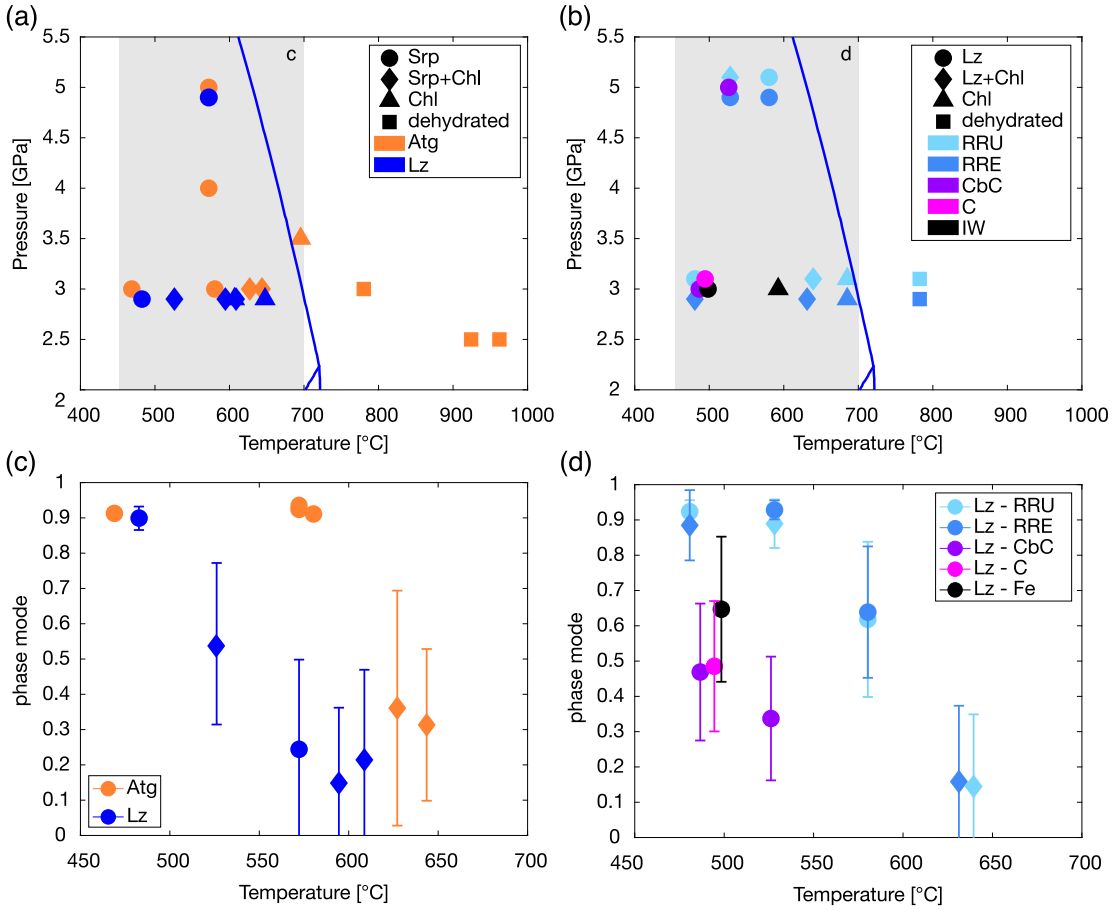

Fig. 2. (a) *P–T* diagram showing unbuffered lizardite- and antigorite-bearing experiments. Different symbols indicate the stable hydrous phase. The (blue) lines indicate the antigorite dehydration of Ulmer & Trommsdorff (1995). The highlighted area marks the temperature range in c. (b) *P–T* diagram of buffered lizardite-bearing samples. The highlighted area marks the temperature range in d. (c) Mode of serpentine in unbuffered lizardite- and antigorite-bearing experiments. The onset of dehydration in lizardite is at lower temperature. (d) Mode of lizardite in buffered experiments. The dehydration is observed at lower temperature in more reducing experiments.

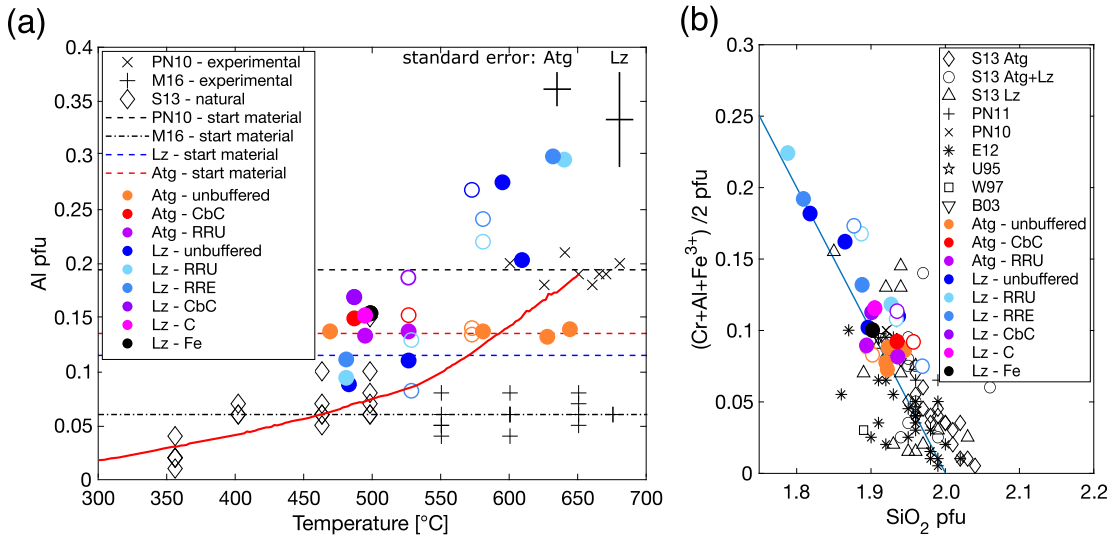

Fig. 3. (a) Al content in serpentine as a function of temperature in experiments of this study (circles) and various literature data (crosses—experiments; diamonds—natural samples). Antigorite stoichiometry is normalised to two tetrahedral sites. Horizontal lines mark the composition of the starting materials. Antigorite does not change its composition during experiments as also shown by other experimental studies. The (red) solid line shows the Al content of antigorite calculated with the new thermodynamic model of this study along the *P–T* path indicated in Fig. 8a (see text for details on the model). (b) Total trivalent cation content is inversely correlated with Si content, implying a coupled substitution. Open symbols of data in this study mark experiments at $P \geq 4$ GPa. Literature data are as follows: B03: Bromiley & Pawley (2003), W97: Wunder & Schreyer (1997), U95: Ulmer & Trommsdorff (1995), E12: Evans *et al.* (2012), PN10/PN11: Padrón-Navarta *et al.* (2010, 2011), M16: Merkulova *et al.* (2016), S13: Schwartz *et al.* (2013).

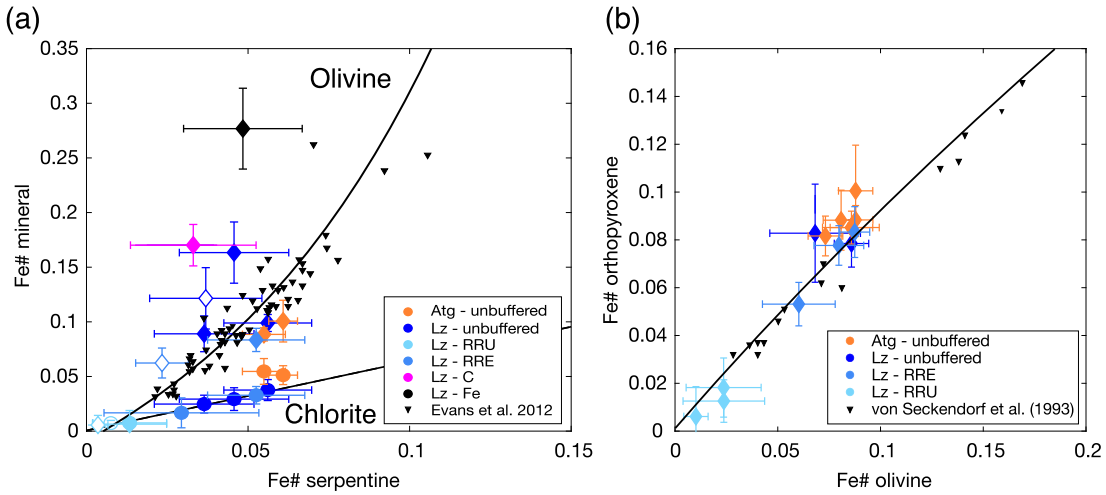

Fig. 4. (a) Fe^{2+}–Mg exchange between serpentine and coexisting olivine (diamonds) and chlorite (circles). Serpentine is more Mg rich with respect to olivine, but more Fe rich with respect to chlorite. Both serpentine and chlorite are corrected for ferric Fe. Black triangle diamonds are data for metamorphic antigorite–olivine pairs from Evans *et al.* (2012), not corrected for ferric Fe. Solid lines show the relation between coexisting phases according to $Fe\#_{ol} = 104\ (Fe\#_{serp})^3 + 3.6412\ (Fe\#_{serp})^2 + 1.7966\ (Fe\#_{serp}) - 0.0094$ and $Fe\#_{chl} = 0.64129\ Fe\#_{serp} + 0.00014$. Open symbols mark experiments performed at $P \geq 4$. (b) Fe^{2+}–Mg exchange between coexisting olivine and orthopyroxene. The data are in good agreement with experimental literature data (von Seckendorff *et al.*, 1993). The relation is given by $Fe\#_{opx} = 0.8772\ (Fe\#_{ol})^3 - 0.8804\ (Fe\#_{ol})^2 + 0.9906\ (Fe\#_{ol}) + 0.0017$. Not shown are experiments in which the olivine and/or orthopyroxene composition is estimated from experiments performed at similar conditions (see main text for explanation).

In sample V1102, which has undergone complete dehydration, a minor amount of Fe^{2+}-bearing garnet can be observed.

While Fe^{3+} in antigorite is exclusively hosted in the octahedral site, lizardite in the starting material contains additional Fe^{3+} in the tetrahedral site (Fig. 5e). The Fe^{3+}/Fe^{tot} ratio of lizardite in the starting material is 0.68(12) (the different serpentine generations in the starting material could not be distinguished in the Mössbauer spectra). In the experimental products, tetrahedral Fe^{3+} was only observed at low temperatures and high $f(O_2)$, and it disappears at higher temperatures and pressure (Figs. B5-3, B5-5). To illustrate, Fig. 5f–h shows Mössbauer spectra of lizardite under various redox conditions at 500 °C. At a low $f(O_2)$ of FMQ-2.2, Fe^{3+} is nearly absent, whereas at high $f(O_2)$ of FMQ+10.8 the majority of Fe in lizardite is ferric, $Fe^{3+}/Fe^{tot} = 0.86(11)$, although the total Fe concentration in serpentinite with respect to the starting material decreased.

Overall, it was possible to both raise and lower the Fe^{3+}/Fe^{tot} ratio of lizardite using different oxygen fugacity buffers, resulting in a consistent dependence of the Fe^{3+}/Fe^{tot} ratio on the $f(O_2)$ as shown in Fig. 6. For antigorite samples, however, this did not occur, and all experimental run products were slightly reduced compared to the starting material, even those performed using the Ru + RuO_2 buffer. The antigorite appears nonetheless to be in equilibrium with coexisting phases (Fig. 4), as discussed later. In the unbuffered experiments, which contained redox sensors, there is a general trend of decreasing Fe^{3+}/Fe^{tot} ratio in serpentine with increasing temperature.

DISCUSSION

In the following we first discuss the phase relations in the experimental products with regard to the state of equilibrium. We then define new Fe^{3+}- and Al-endmembers for lizardite and antigorite, for which we determine standard state Gibbs energies from mineral equilibria and compositions in our experimental products. Finally, we implement the new endmembers into the Gibbs energy minimisation software package Perple_X (Connolly, 2005), which allows changes in the redox potential of subducted serpentinites during the lizardite to antigorite phase transformation and antigorite dehydration to be examined.

Attainment of equilibrium

Variations of the Fe concentration in antigorite with run temperature seem to indicate that Fe^{2+}–Mg exchange with other phases is at least approached, whereas Fe^{3+} and Al concentrations of antigorite change only slightly on experimental scales (Figs. 3a and 6a). There is a consistent decrease in the Fe^{3+} concentration of antigorite between the starting material (~0.05 Fe^{3+} cations pfu) and the experimental products (~0.03 Fe^{3+} cations pfu), but insignificant variation with respect to imposed oxygen buffers (Fig. 6a). Similarly, the Al concentration of antigorite remains constant in experimental run products, even where it coexists with chlorite (V1105, V1111), in contrast to trends observed in natural samples (Schwartz *et al.*, 2013). Similar behaviour of antigorite coexisting with chlorite was also observed by Padrón-Navarta *et al.* (2010) and Merkulova *et al.* (2016). We hypothesise that the modulation of the tetrahedral and octahedral layers in antigorite (Capitani & Mellini, 2004) is responsible for low diffusivity of the tetrahedrally coordinated cations, due to a reversal of the tetrahedral layer. The charge coupling between tetrahedral Al and octahedral Fe^{3+} appears to be rate limiting for variations in the Fe^{3+} abundance in the octahedral site. By contrast, faster diffusivities are expected for octahedrally coordinated cations, and this allows the Fe^{2+}–Mg exchange between antigorite and coexisting silicates to approach equilibrium during experiments (Fig. 4), which allows us to write mineral equilibria and solve them for thermodynamic parameters. Similarly, we observe an increase in the Fe concentration of the coexisting (Ir,Fe) redox sensor in unbuffered samples. We assume that the (Ir,Fe) redox sensor equilibrates with an $f(O_2)$ imposed by the antigorite composition, and this allows the relationship between $f(O_2)$ and the antigorite Fe^{3+}/Fe^{tot} ratio to be determined.

In the experiments with lizardite serpentinite, the lizardite did not transform to antigorite at the experimental conditions, which are well above the expected transformation temperature of approximately 300 °C (Schwartz *et al.*, 2013). Although lizardite

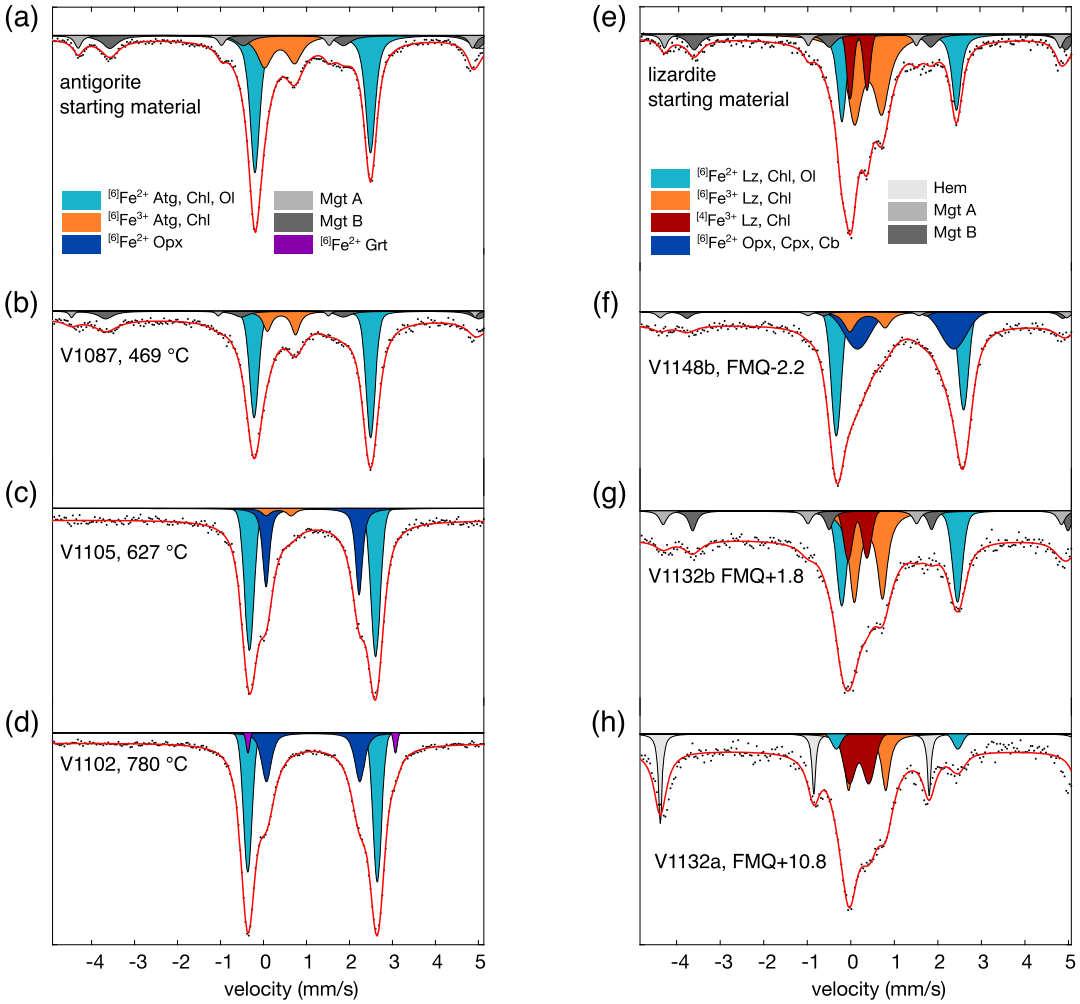

Fig. 5. Room temperature Mössbauer absorption spectra of representative samples. (a) The antigorite serpentinite starting material has ferric Fe only on the octahedral site. (b to d) With increasing temperature, magnetite and serpentine disappear. Increasing proportions of olivine, orthopyroxene and garnet are observed. (e) The lizardite serpentinite starting material also contains tetrahedral ferric Fe. (f to h) With increasing $f(O_2)$, the Fe^{3+}/Fe^{tot} ratio of lizardite increases. Note the broad peaks in experiment V1148b most probably indicating a poorly crystallised carbonate and olivine–pyroxene intergrowth.

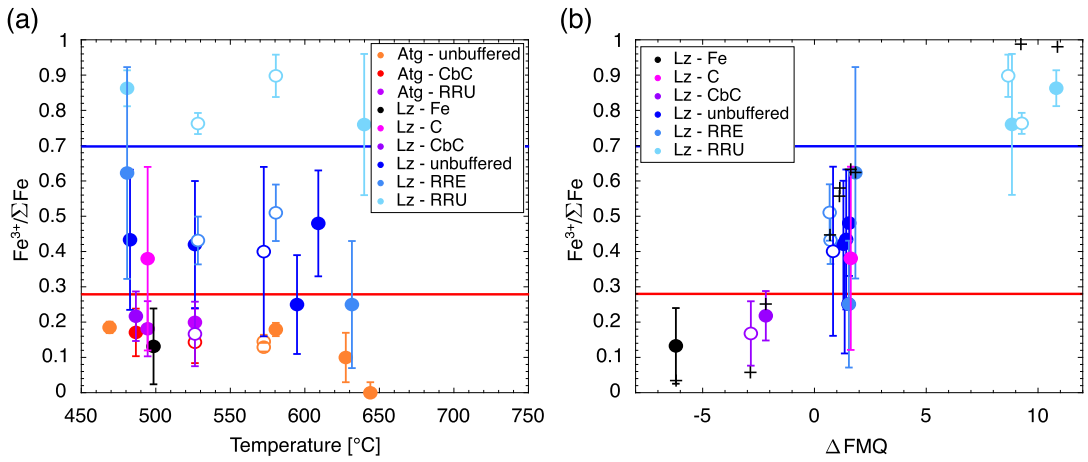

Fig. 6. Fe^{3+}/Fe^{tot} ratio of serpentine in experimental run products. (a) The Fe^{3+}/Fe^{tot} ratio in antigorite decreases only above 600 °C and is independent of the pressure and the buffer component added. Lizardite shows a decrease with increasing temperature at a fixed $f(O_2)$ over the entire experimental temperature range. (b) The Fe^{3+}/Fe^{tot} ratio of lizardite is also strongly dependent on the $f(O_2)$. Note that the experiment at ΔFMQ <−5 was buffered with Fe metal and probably did not fully equilibrate. The Fe^{3+}/Fe^{tot} ratio in this experiment might thus be even lower. The black crosses represent values obtained with the new solid solution models of this study for the experimental conditions.

Table 3: Endmembers used for serpentine solid solution models in this study

Endmember		Formula	Linear combination	DQF (*a*, *b*, *c*)	Ref.
Mg–lizardite	Lz	$Mg_3Si_2O_5(OH)_4$	Known endmember	–	1
Fe^{2+}–lizardite	fLz	$Fe_3Si_2O_5(OH)_4$	1 Lz—1 Tlc + 1 fTlc	−21 000, 0, 0	2
Fe^{3+}–lizardite	f3Lz	$Mg_2Fe^{3+}\|AlSi\|O_5(OH)_4$	1 Lzts—0.5 Grs + 0.5 Adr	−18 000, 0, −0.1	3
Al–lizardite	Lzts	$Mg_2Al\|AlSi\|O_5(OH)_4$	1 Lz—1 Tlc + 1 Tlcts	−37 000, 0, 0.1	3
Ordered lizardite	oLz	$Mg_2Fe\|Si_2\|O_5(OH)_4$	1 Lz—1/3 Tlc + 1/3 fTlc	−9000, 0, 0	2
Mg–antigorite	Atg	$Mg_{48}Si_{34}O_{85}(OH)_{62}$	Known endmember	–	1
Fe^{2+}–antigorite	fAtg	$Fe_{48}Si_{34}O_{85}(OH)_{62}$	1 Atg—16 Tlc + 16 fTlc	−350 000, 0, 0	2
Fe^{3+}–antigorite	f3Atg	$Mg_{31}Fe^{3+}{}_{17}\|Al_{17}Si_{17}\|O_{85}(OH)_{62}$	1 Atgts—8.5 Grs + 8.5 Adr	−127 000, 0, −3.4	3
Al–antigorite	Atgts	$Mg_{31}Al_{17}\|Al_{17}Si_{17}\|O_{85}(OH)_{62}$	1 Atg—17 Tlc + 17 Tlcts	−450000, 0, 0	3
Ordered antigorite	oAtg	$Mg_{31}Fe_{17}\|Si_{34}\|O_{85}(OH)_{62}$	1 Atg—17/3 Tlc + 17/3 Tlcts	−124 000, 0, 0	2

Abbreviations from Whitney & Evans (2010); Tlcts corresponds to the Talc-Tschermak endmember. *a*, *b*, and *c* are DQF parameters, whereby DQF = $a + bT + cP$, with *a* in J/mol, *b* in J/mol K and *c* in J/mol bar. The value of DQF of the Fe^{2+}-endmembers was modified to match the Fe^{2+}–Mg partitioning in our experiments. References: 1—Holland & Powell (2011), 2—modified from Evans & Frost (2021), 3—this study.

in the experiments is metastable with respect to antigorite, it nonetheless appears to maintain chemical equilibrium within the surrounding assemblage, and it dehydrates at temperatures comparable with those of antigorite dehydration. Lizardite does not have a reversal of the tetrahedral layers, which likely promotes faster equilibration of the trivalent cations.

A new thermodynamic model for ferric Fe serpentine

In our experiments, antigorite hosts Fe^{3+} in the octahedral site, which is charge balanced by Al in the tetrahedral site. Similarly, Fe^{3+} preference for the octahedral site in lizardite has been documented by our high-pressure experiments, although some Fe^{3+} enters the tetrahedral site at low temperatures and high oxygen fugacities. We derive a thermodynamic solution model for Fe^{3+} and Al in lizardite and antigorite by introducing four new endmembers (f3Lz, Lzts, f3Atg, Atgts; Table 3). The formula unit for antigorite was chosen to correspond to the $m = 17$ polysome and is hereafter normalised to two tetrahedral sites in order to facilitate comparison with the lizardite endmembers. The relationship between the antigorite and lizardite solid solutions is as follows:

$$\text{Atg} = \text{Lz} - 3/17\ (\text{Fo} + \text{H}_2\text{O} - 0.5\ \text{En}). \quad (7)$$

In order to calculate the standard state Gibbs energy of the new endmembers, the following equilibria between minerals in our run products are formulated for f3Lz and Lzts:

$$\text{f3Lz} = 1/2\ \text{Mag} + 1/2\ \text{Clin} - 1/4\ \text{Fo} - 1/4\ \text{Fa} \quad (8)$$

$$\text{f3Lz} = 1/3\ \text{Mag} + 1/12\ \text{O}_2 + 1/2\ \text{Clin} - 1/4\ \text{En} \quad (9)$$

$$\text{f3Lz} = 1/2\ \text{Fa} + 1/2\ \text{Fo} + 1/2\ \text{Clin} + 1/4\ \text{O}_2 - 3/4\ \text{En} \quad (10)$$

$$\text{Lzts} = \text{Clin} - \text{Fo} - 1/2\ \text{En} - 2\ \text{H}_2\text{O} \quad (11)$$

$$\text{Lzts} = \text{Clin} - \text{Lz}. \quad (12)$$

The two following equilibria are analogous to Eqs. (8) and (9) but written with hematite for higher $f(O_2)$ experiments:

$$\text{f3Lz} = 3/4\ \text{Hem} + 1/2\ \text{Clin} - 1/8\ \text{O}_2 - 1/4\ \text{Fo} - 1/4\ \text{Fa} \quad (13)$$

$$\text{f3Lz} = 1/2\ \text{Hem} + 1/2\ \text{Clin} - 1/4\ \text{En}. \quad (14)$$

The equilibria for the antigorite endmembers are obtained by substituting Eq. (7) into Eqs. (8) to (14). The Gibbs energy of the new endmembers is then obtained by solving the equilibrium condition:

$$0 = \Delta_r G = \Sigma \upsilon_i \left(G_i^o + RT\ \ln\ a_i\right), \quad (15)$$

where G_i^o is the standard Gibbs energy of endmember *i* at the temperature and pressure of interest, υ_i the stoichiometric coefficient of endmember *i* in the equilibrium relation and a_i is the activity of endmember *i*. The Gibbs energies of the coexisting phases were calculated using the equation of state and dataset of Holland & Powell (2011), version DS622. We used the equation of state for H_2O of Pitzer & Sterner (1994) with activity of H_2O set to 1. Decreasing the activity to 0.9 did not significantly affect the resulting Gibbs energy for any of the serpentine endmembers. Hematite was considered to be an endmember phase due to its almost pure composition. We applied a three-site regular mixing model for magnetite, a simple symmetric model for olivine and a full order–disorder solution model for orthopyroxene according Jennings & Holland (2015). Chlorite was treated as a non-ideal solid solution following White *et al.* (2014). The uncertainty arising from ferric Fe in chlorite was considered negligible based on its low ferric Fe content as obtained from our Mössbauer spectroscopy results. For experiments in which olivine, orthopyroxene and chlorite were not measured, we constrained their expected equilibrium composition based on Fe^{2+}–Mg exchange (Fig. 4) and fixed the chlorite Al concentration to 1.6 Al pfu.

For serpentine, we use an ordered model in line with solution models for other sheet silicates (e.g. Tajčmanová *et al.*, 2009; White *et al.*, 2014; Evans & Powell, 2015): Al and Fe^{3+} mix on one octahedral site (*M*1), and tetrahedral Al mixes on half of the tetrahedral sites (*T*1), i.e., on one tetrahedral site. Fe^{2+}–Mg exchange is enabled on all octahedral sites (*M*0 and *M*1). The corresponding activity expressions for the Al- and Fe^{3+}-endmembers are as follows:

$$a_{\text{srpts}} = (X_{\text{Mg(M0)}})^{M-1}\ X_{\text{Al}(M1)} X_{\text{Al}(T1)} \quad (16)$$

$$a_{\text{f3srp}} = (X_{\text{Mg(M0)}})^{M-1}\ X_{\text{Fe}^{3+}(M1)} X_{\text{Al}(T1)}, \quad (17)$$

where *M* is the total number of octahedral cations in the formula unit, i.e., 3 for lizardite and 2.824 for antigorite. The site fractions are calculated from the mineral formula (apfu) as follows:

$$X_{\text{Mg(M0)}} = \text{Mg}_{(M0)}/(M-1) = \text{Mg\#} \quad (18)$$

$$X_{\text{Fe}^{3+}(M1)} = \text{Fe}^{3+} \quad (19)$$

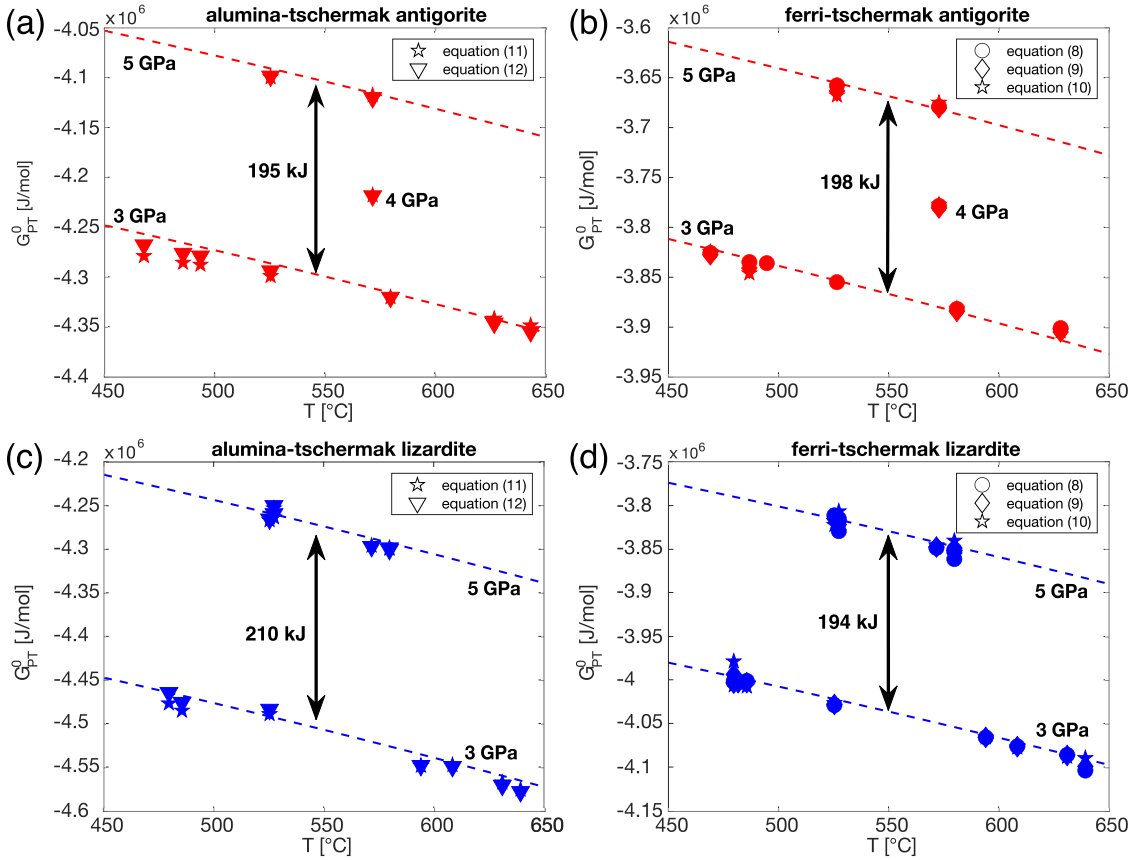

Fig. 7. The Gibbs energy of the new Al- and Fe^{3+}-endmembers for antigorite (a, b) and lizardite (c, d). The symbols mark experimentally determined free energies obtained by fitting Eqs. (8)–(12) to the experimental results. The lines show the free energy obtained from linear combinations given in Table 3.

$$X_{Al(M1)} = Al^{[6]} \quad (20)$$

$$X_{Al(T1)} = Al^{[4]}. \quad (21)$$

The partitioning of Al between the octahedral and tetrahedral sites is based on charge balance by

$$Al^{[4]} = 1/2\,[Fe^{3+} + Al^{tot}] \quad (22)$$

$$Al^{[6]} = Al^{tot} - Al^{[4]}. \quad (23)$$

Fig. 7a, b shows the resulting standard state Gibbs energy of the Atgts and f3Atg endmembers at various pressures. For both endmembers, we obtain a pressure dependence of the Gibbs energy of about 100 kJ/GPa, which corresponds to the molar volumes of 97(1) cm^3/mol and 99(1) cm^3/mol for Atgts and f3Atg, respectively. These values agree with the standard molar volume of 97 cm^3/mol obtained for natural Al- and Fe^{3+}-bearing antigorite (Hilairet *et al.*, 2006). A similar pressure dependency is found for the lizardite endmembers Lzts and f3Lz (Fig. 7c, d), leading to the molar volumes of 105(2) and 97(1) cm^3/mol, respectively. Due to the limited number of experiments, it is, however, not possible to obtain the enthalpic and entropic contribution to the Gibbs energy of these endmembers independently. Therefore, in order to use the new endmembers at variable pressures and temperatures, we constrain their Gibbs energy as linear combinations of known endmembers combined with a perturbation term (DQF, Darkens Quadratic Formalism). The linear combinations were chosen to be functions of various talc endmembers, to remain as close as possible to the sheet silicate crystal structure (Table 3). Because Al and Fe^{3+} are minor constituents in serpentine, we assume that non-ideal interactions are not changing significantly with composition and are, therefore, accounted for by the Henrian standard state for the Fe^{3+}- and Al-endmembers. The values of the DQF term were obtained by minimising the difference between the Gibbs energy of the linear combination and the standard state Gibbs energy of the endmembers obtained from the experiments with the following constraints: (1) serpentine is only stable at temperatures ≤650 °C, i.e., the free energy of the serpentine assemblage must be higher than the chlorite assemblage at higher temperatures, (2) the Al and Fe^{3+} concentrations are pressure independent; (3) Al, Fe^{3+}, Mg–Fe^{2+} exchange must fit the experimental data. The resulting Gibbs energy is shown in Fig. 7, and DQF parameters are summarised in Table 3. A comparison between the new model and previous serpentine solution models can also be found in the supporting information B-3. All input files used for the Perple_X models in this study are available in supporting information B-6.

Serpentine phase transformation during subduction

The new serpentine endmembers and their thermodynamic properties allow us to model and discuss various features of the lizardite to antigorite phase transformation in nature. Since the two serpentine minerals are not strictly polymorphs of each other, the phase transformation involves additional phases to account for differences in Al, Fe^{3+} and octahedral/tetrahedral ratio. During the phase transformation, the bulk redox budget can either be retained, i.e., a closed system with a constant amount of oxygen, or changed, for example, through reaction

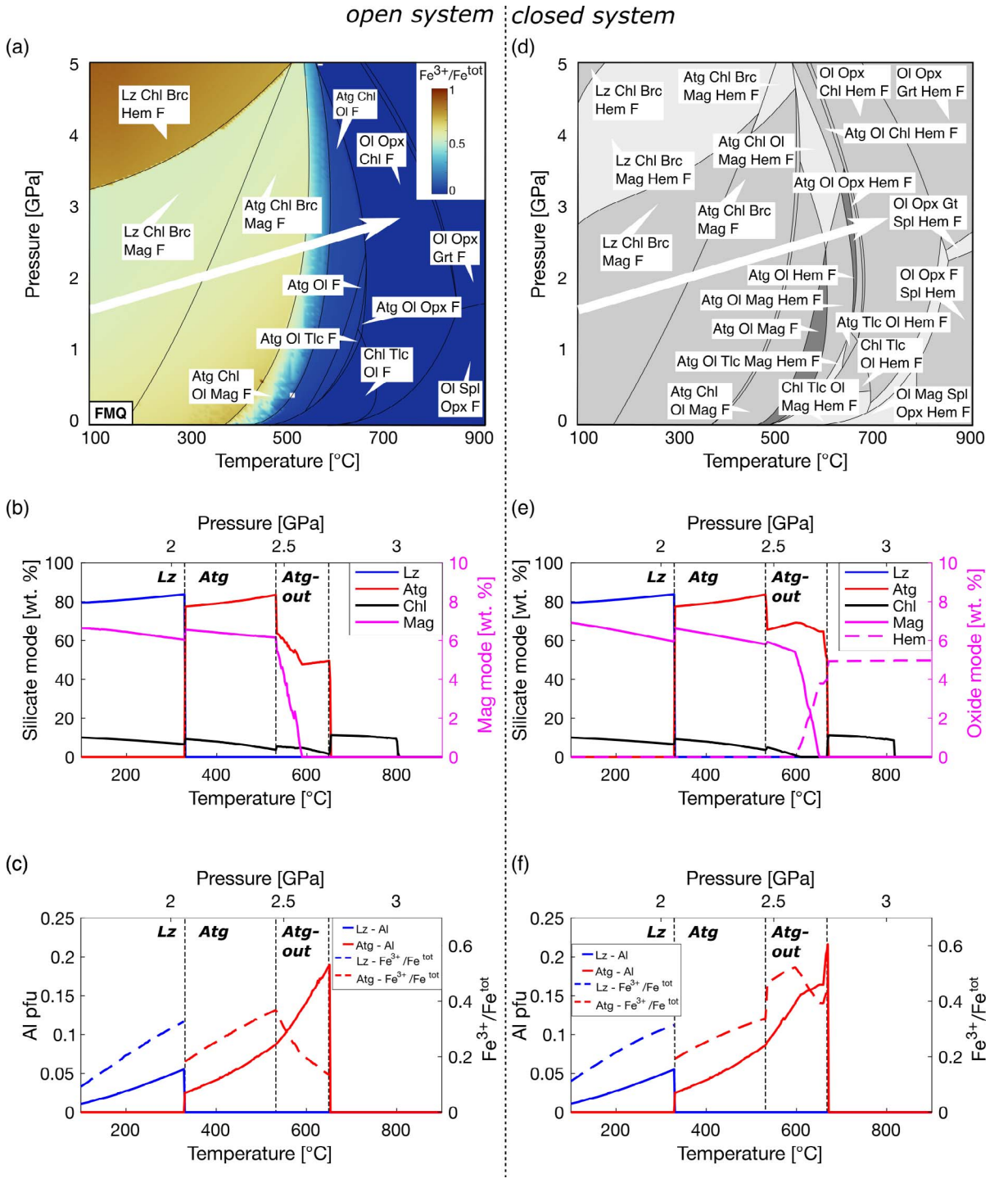

Fig. 8. (a) The lizardite to antigorite phase transformation calculated with the new solution models implemented in Perple_X for the bulk composition 97 wt. % lizardite + 3 wt. % magnetite (supporting information B-3). The *P*–*T* pseudosection is buffered at FMQ. The colour code indicates the bulk Fe^{3+}/Fe^{tot} ratio. The white arrow marks the *P*–*T* path used in b and c. (b) Phase modes of the sheet silicates lizardite, antigorite and chlorite, and oxide along the *P*–*T* path from a. Indicated are also major reactions such as the lizardite to antigorite phase transformation and the antigorite-out reaction. (c) The Al and Fe^{3+}/Fe^{tot} ratio of lizardite and antigorite along the *P*–*T* path from a. (d to f) The same calculation for a closed system, i.e., with a fixed O_2 content of 0.5 wt. %, giving rise to a bulk Fe^{3+}/Fe^{tot} content of 0.55.

with other volatile components, in an open system. The $f(O_2)$ could be potentially buffered in an open system, rather than the bulk Fe^{3+}/Fe^{tot} ratio. Fig. 8a shows a pressure–temperature (*P*–*T*) pseudosection buffered at FMQ for the bulk composition 97 wt. % lizardite +3 wt. % magnetite (Table B3-1). In this open system, the lizardite to antigorite phase transformation is observed at 300 °C at 2 GPa, in agreement with Schwartz *et al.* (2013), although with a positive volume change. There is no significant difference in the bulk Fe^{3+}/Fe^{tot} ratio predicted in the lizardite vs the antigorite stability field and magnetite forms during the serpentine phase transformation (Fig. 8b) as a consequence of the antigorite Fe^{3+} concentration being lower than that of lizardite at equilibrium (Fig. 8c). In an open system buffered at specific $f(O_2)$ conditions, the transformation, therefore, has no significant effect on the

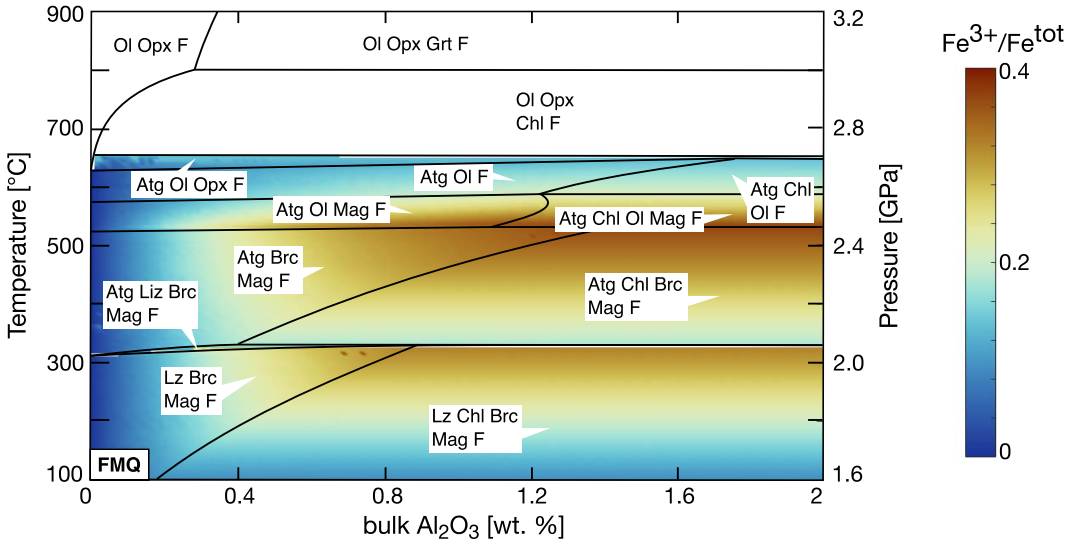

Fig. 9. Compositional diagram showing the effect of bulk Al_2O_3 on the redox potential. The bulk composition (97 wt. % lizardite + 3 wt. % magnetite, supporting information B-3) changes from 0 to 2 wt. % Al_2O_3. The system is buffered at FMQ. Colour code shows the lizardite and antigorite Fe^{3+}/Fe^{tot} ratio.

redox budget and follows near identical behaviour to that of the closed system calculated with a fixed bulk Fe^{3+}/Fe^{tot} content of 0.55 (Fig. 8e, f). This contrasts, however, with studies of natural serpentinites that show a decrease in redox budget upon the lizardite to antigorite phase transformation (Reynard *et al.*, 2022). Comparison of lizardite- and antigorite-bearing natural samples even suggests the consumption of magnetite together with a significant decrease in the bulk Fe^{3+}/Fe^{tot} ratio upon this phase transformation (Debret *et al.*, 2014, 2015; Brounce *et al.*, 2019; Mayhew & Ellison, 2020). Thus, rather than being buffered at specific $f(O_2)$ conditions throughout the phase transformation, these natural samples appear to experience open-system reduction. The reduction of bulk ferric Fe could have been achieved through the oxidation of organic carbon or sulphides, which may have been kinetically inhibited up to the temperature of the transformation. However, since the sulphur and carbon content in serpentinites is not particularly high (Alt *et al.*, 2013; Merkulova *et al.*, 2017), it remains questionable whether significant reduction in this way and the release of oxidising fluids is the norm in all subduction zones or whether the redox budget of the system, i.e., the total amount of oxygen, tends to remain relatively constant. It is also possible that at the conditions of this transformation, continued serpentinisation at greater depth results in the release of H_2, which then causes reduction (Vitale Brovarone *et al.*, 2017). Nevertheless, there seems to be no process intrinsic to the serpentine transformation itself that should lead to a decrease in the bulk Fe^{3+}/Fe^{tot} ratio of the rock.

The main difference between the open ($f(O_2)$ buffered) and closed (fixed bulk Fe^{3+}/Fe^{tot} ratio) systems occurs at the antigorite dehydration reaction. In the open system, the fixed $f(O_2)$ causes the bulk Fe^{3+}/Fe^{tot} ratio to decrease upon antigorite dehydration. In the closed system, however, chlorite is not able to accommodate all the antigorite Fe^{3+} as it breaks down and hematite starts to form, which causes the $f(O_2)$ to rise across the antigorite dehydration.

The effect of the bulk aluminium concentration

Fig. 8c, f also shows a strong increase of the Al concentration in both lizardite and antigorite with increasing temperature. This is in agreement with the variations in Al concentration found for natural serpentinites (compare Figs 3a and B3-1). However, since Fe^{3+} in antigorite is incorporated in the octahedral site and charge balanced by tetrahedral Al, we expect that changing the Al concentration of serpentine will impact the Fe^{3+} concentration of antigorite. This hypothesis may be extended to lizardite, as tetrahedral Fe^{3+} is only a minor component (Evans *et al.*, 2012), present in our experiments only below 500 °C, at intermediate to high $f(O_2)$. It should be noted, however, that the findings discussed below strictly only hold for the case that no other Fe^{3+} substitution mechanisms occur, such as the formation of octahedral vacancies.

In Fig. 9 we calculate the serpentine Fe^{3+}/Fe^{tot} ratio for the bulk composition 97 wt. % lizardite + 3 wt. % magnetite (Table B3-1) with variable bulk Al_2O_3 concentration from 0 to 2 wt. % buffered at FMQ. At low bulk Al concentrations, serpentine is the sole host of aluminium as chlorite only becomes stable at higher bulk Al concentrations. These findings are qualitatively identical to the calculation by Padrón-Navarta *et al.* (2013). At these conditions, the Fe^{3+}/Fe^{tot} ratio of serpentine depends strongly on the bulk Al concentration but is essentially independent of temperature. In the serpentine + chlorite stability fields, the Al exchange between the two phases enables the Al concentration and the Fe^{3+}/Fe^{tot} ratio of serpentine to vary as a function of temperature. It is plausible, therefore, that a serpentinite with initially low Al concentration will have a Fe^{3+}/Fe^{tot} ratio limited by the Al content. On the other hand, a serpentinite with an initially high Al concentration will contain coexisting serpentine and chlorite and the serpentine Fe^{3+}/Fe^{tot} ratio will change during prograde subduction metamorphism as shown in Fig. 9. Serpentinites with intermediate Al concentrations are expected to have chlorite stable during low-grade subduction metamorphism, and the Fe^{3+}/Fe^{tot} ratio will be dictated by internal redox buffers, such as coexisting magnetite + olivine + antigorite. With increasing temperature, Al partitions progressively into the serpentine phase until chlorite is completely consumed, at which point the serpentine Fe^{3+}/Fe^{tot} ratio will remain constant. This is in agreement with our antigorite-bearing experiments, where the antigorite Fe^{3+} concentration remained constant as a result of the Al concentration not changing due to sluggish reaction kinetics, even in the presence of high $f(O_2)$ buffers. This relationship with Al

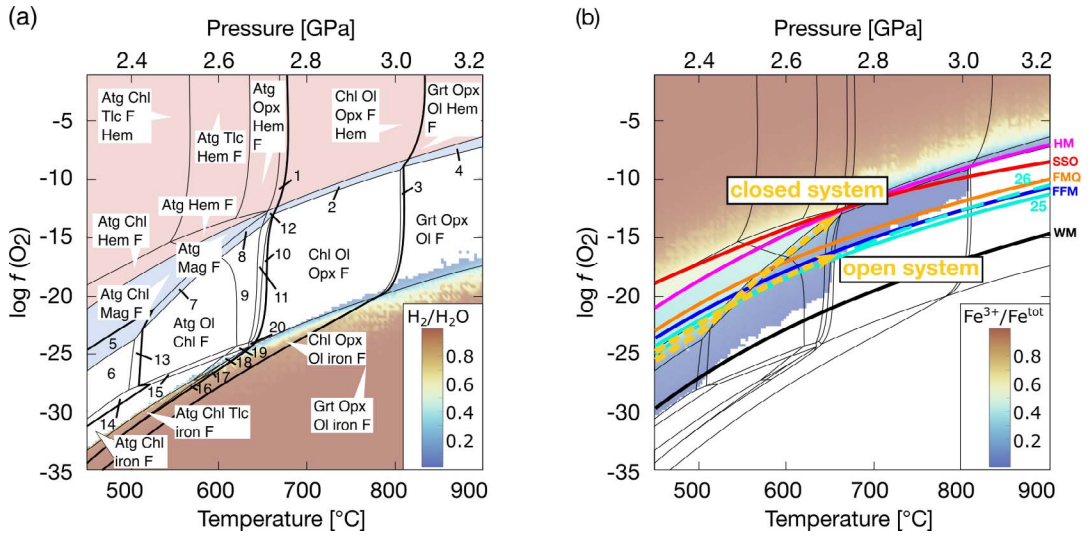

Fig. 10. Phase diagram section calculated along a subduction path for the bulk composition 98 wt. % antigorite + 2 wt. % magnetite (supporting information B-3). (a) The excess Fe phase changes from Fe metal at low $f(O_2)$ conditions to an excess Fe phase absent field into magnetite and hematite at high $f(O_2)$. Dehydration reactions (brucite-out, antigorite-out, chlorite-out) are highlighted by thick lines. The composition of the fluid in equilibrium with Fe metal is highlighted. Numbers correspond to (1) Atg, Opx, Ol, Hem, F; (2) Chl, Opx, Ol, Mag, F; (3) Chl, Opx, Ol, Grt, F; (4) Opx, Ol, Grt, Mag, F; (5) Atg, Chl, Br, Mag, F; (6) Atg, Chl, Br, F; (7) Atg, Chl, Ol, Mag, F; (8) Atg, Ol, Mag, F; (9) Atg, Ol, F; (10) Atg, Chl, Opx, Ol, F; (11) Atg, Opx, Ol, F; (12) Atg, Opx, Ol, Mag, F; (13) Atg, Chl, Ol, Br, F; (14) Atg, Chl, Br, iron, F; (15) Atg, Chl, Ol, iron, F; (16) Atg, Chl, Opx, iron, F; (17) Atg, Opx, iron, F; (18) Atg, iron, F; (19) Atg, Ol, iron, F; (20) Atg, Opx, Ol, iron, F. (b) The same diagram colour coded for bulk Fe^{3+}/Fe^{tot} ratio. Coloured lines mark the $f(O_2)$ buffers (wüstite–magnetite (WM), FFM, FMQ and HM calculated; SSO from Evans & Frost, 2021) as well equilibria (25) and (26). The two $f(O_2)$ evolution scenarios (scenario (1)—$f(O_2)$ buffered open system; scenario (2)—closed system) discussed in the text are shown as yellow arrows.

likely has consequences for the interpretation of other antigorite experimental studies, as the Fe^{3+} concentration in antigorite will not change during experimental time scales of several days, even when external redox buffers are applied.

Evolution of the oxygen fugacity in subducting serpentinites

As argued in the previous paragraph, the bulk composition of subducted serpentinites can have a significant effect on the $f(O_2)$ during progressive metamorphism. In Fig. 10a we calculate the phase relations for the bulk composition 98 wt. % antigorite + 2 wt. % magnetite (Table B3-1) along the *P*–*T* path of the northern Honshu subduction zone (Syracuse *et al.*, 2010).

At the lowest computed $f(O_2)$ conditions, antigorite is stable with Fe metal and the system does not contain any Fe^{3+} (compare Fig. 10b). The dehydration temperature of antigorite is predicted to decrease at such low $f(O_2)$ conditions to <650 °C, mainly because a significant H_2 component increases the stability of the fluid phase. At a log $f(O_2) = -30$, the dehydration of antigorite takes place at 530 °C and the fluid has a molar H_2/H_2O ratio of 0.9. This is consistent with the experiments performed with Fe metal, which showed a clear decrease in serpentine stability due to such redox-induced dehydration (Figs. 1d and 2d). Serpentinites can contain (Fe,Ni)-sulphides and native metals (Frost, 1985; Merkulova *et al.*, 2017). While it was already proposed that the onset of dehydration might be controlled by chemical heterogeneities (Plümper *et al.*, 2017; Huber *et al.*, 2022), we now propose local redox gradients to have a similar effect. Consequently, dehydration in serpentinites might first start in the vicinity of these highly reduced phases during subduction metamorphism.

For a bulk Fe^{3+}/Fe^{tot} ratio <0.2, all Fe^{3+} partitions into antigorite. Magnetite is stable at bulk Fe^{3+}/Fe^{tot} ratios of 0.2–0.4. At higher $f(O_2)$ conditions, hematite becomes the main host of Fe^{3+} and the dominant Fe-bearing phase. This causes the antigorite stability field to expand slightly to higher temperature, owing to its almost pure Mg-endmember composition.

The evolution of the $f(O_2)$ during serpentinite subduction metamorphism can be investigated considering two scenarios: (1) where the $f(O_2)$ is buffered, similar to the open-system example in Fig. 8a–c, such as through the presence of carbon- and/or sulphur-bearing components; (2) where the bulk Fe^{3+}/Fe^{tot} ratio is fixed (Fig. 10b).

In partially serpentinised peridotites, the presence of relict olivine, orthopyroxene and magnetite could buffer the $f(O_2)$ to some extent according to the equilibrium fayalite–ferrosilite–magnetite (FFM):

$$2\ Fe_2SiO_4 + 1/3\ O_2 = Fe_2Si_2O_6 + 2/3\ Fe_3O_4. \quad (24)$$

However, changes in Mg–Fe^{2+} substitution with pressure and temperature will affect the $f(O_2)$ of the equilibrium. The presence of either graphite and/or carbonate (Alt *et al.*, 2013) in partially to fully serpentinised peridotites also has the potential to act as a redox buffer via the equilibria (Eberhard *et al.*, 2023):

$$2\ Mg_2SiO_4 + 2\ C + 2\ O_2 + CaMg(CO_3)_2 = CaMgSi_2O_6 + 4\ MgCO_3 \quad (25)$$

$$Mg_{48}Si_{34}O_{85}(OH)_{62} + 20\ MgCO_3 = 20\ C + 20\ O_2 + 34\ Mg_2SiO_4 + 31\ H_2O. \quad (26)$$

In a system buffered by graphite and magnesite, Eq. (26), a relatively high Fe^{3+}/Fe^{tot} ratio of 0.4 is predicted at temperatures below 500 °C. But as can be seen in Fig. 10b, the bulk rock progressively reduces upon further subduction, and complete reduction of Fe^{3+} is reached at 650 °C. Serpentinites containing graphitic material will, therefore, be buffered at an $f(O_2)$ below the magnetite stability field (Fig. 10b). Such buffered behaviour is consistent with experimental observations (Merkulova *et al.*, 2017) and natural serpentinite assemblages (Debret *et al.*, 2014, 2015) that record a decrease in the Fe^{3+}/Fe^{tot} ratio of serpentinites with increasing temperature and, therefore, likely reflect open-system

behaviour, where the $f(O_2)$ is buffered or influenced by other redox reactions. In experiments, this may result from the $f(O_2)$ being buffered by a graphite furnace, with reduction of the sample facilitated by hydrogen diffusing through the capsule wall. On the other hand, experiments performed with a $LaCrO_3$ heater that preserve the intrinsically high $f(O_2)$ indeed do not show reduction, but hematite is formed instead (Maurice *et al.*, 2020). In natural samples, it was proposed that hydrogen released through high-temperature serpentinisation could serve as a reducing agent (Vitale Brovarone *et al.*, 2017), or alternatively, fluids equilibrated with adjacent carbonaceous sediments could buffer the $f(O_2)$.

In the second scenario, $f(O_2)$ is controlled by a constant bulk Fe^{3+}/Fe^{tot} ratio of the serpentinite assemblage, which equates to closed system behaviour. If we consider a typical serpentinite bulk Fe^{3+}/Fe^{tot} ratio of 0.4 (Mayhew & Ellison, 2020), then at 500 °C, the log $f(O_2)$ is −24 (Fig. 10b), within the magnetite + brucite stability field. This is consistent with natural brucite-bearing serpentinites, which have relatively low $f(O_2)$ confirmed by observations of H_2 in fluid inclusions under greenschist facies conditions (Peretti *et al.*, 1992). With increasing *P*–*T* conditions, the $f(O_2)$ of the assemblage increases above the FMQ buffer and reaches hematite–magnetite (HM) −0.5 upon antigorite dehydration; this $f(O_2)$ progression is qualitatively similar to that proposed by Piccoli *et al.* (2019). In order to exceed the HM buffer, however, a bulk Fe^{3+}/Fe^{tot} greater than 0.6 would be required (cf. Mayhew & Ellison, 2020). At least based on natural serpentinites, this would seem unlikely if the bulk Fe^{3+}/Fe^{tot} ratio routinely drops from ∼0.7 to about ∼0.3 upon the lizardite to antigorite phase transformation (Reynard *et al.*, 2022). On the other hand, if the system remains mainly closed throughout subduction, the initially high redox potential of many serpentinites (Debret *et al.*, 2015; Brounce *et al.*, 2019) could be retained through the lizardite–antigorite phase transformation (Fig. 8d–f). Nevertheless, it seems that for more typical ranges of serpentinite bulk Fe^{3+}/Fe^{tot} ratio (0.3–0.5), that during closed system antigorite dehydration, the $f(O_2)$ is likely to be constrained over a relatively narrow range between FMQ-1 and HM (FMQ+3). This is consistent with the determinations of Evans & Frost (2021) who argued that the $f(O_2)$ of subducting serpentinites would be in the range ΔFMQ-2 to +1 at the brucite-out reaction and ΔFMQ+1 to +4 at the antigorite-out boundary. It has been proposed that SO_2 or aqueous sulphate species dissolved in dehydrating serpentinite-derived fluids have the potential to oxidise the mantle wedge (Debret *et al.*, 2014; Debret & Sverjensky, 2017). However, it is noteworthy that the

$$2\,H_2S + 3O_2 = 2SO_2 + 2H_2O \text{ (SSO)} \quad (27)$$

equilibrium, based on the thermodynamic calculations of Evans & Frost (2021), is almost coincident with the HM buffer at conditions of antigorite dehydration. Similar calculations involving aqueous sulphate species give an equivalent $f(O_2)$ approximately 1 log unit lower (Evans & Frost, 2021), but it must be appreciated that these calculations involve significant extrapolations of equation of state properties and have uncertainties that are difficult to constrain. Nevertheless, given that the $f(O_2)$ would have to be above SSO to be dominated by SO_2 rather than H_2S, it is likely that only the most oxidised serpentinites produce fluids capable of oxidising the arc mantle source. In their experimental study, Iacovino *et al.* (2020) proposed that fluids released through antigorite breakdown can oxidise the mantle wedge through the reduction of H^+ to H_2 without the involvement of sulphur species. Alternative sources for oxidising agents could be in altered oceanic crust (Walters *et al.*, 2020), sediment-derived fluids (Padrón-Navarta *et al.*, 2023) or hydrous silicate melts (Tiraboschi *et al.*, 2023).

CONCLUSIONS

In this study we performed experiments on antigorite and lizardite serpentinite assemblages at various *P*–*T*–$f(O_2)$ conditions. Mineral chemical variations illustrate that the composition of lizardite changed as a function of experimental conditions, ranging from 480 to 650 °C at 3 to 5 GPa and log $f(O_2)$ of −26.4 to −4.6, whereas the composition of antigorite remained almost constant. We argued that this is due to sluggish kinetics on experimental time scales of several days. This has important consequences for many experimental studies focusing on the composition of antigorite at various *P*–*T*–$f(O_2)$ conditions, as antigorite is unlikely to change composition, at least in trivalent cations, to attain equilibrium. Since, however, the coexisting silicates appear to be in equilibrium with antigorite in our experiments, we can write mineral equilibria and deduce thermodynamic parameters for antigorite. Lizardite is shown to remain metastable above the lizardite to antigorite transformation, and both phases display a similar stability field.

From our experiments, we have estimated the Gibbs energy of new Fe^{3+}- and Al-Tschermak serpentine endmembers, and the new solid solution model has been used to calculate the phase equilibria of serpentinites as a function of *P*–*T*–$f(O_2)$ conditions and bulk composition. The lizardite to antigorite phase transformation at redox-buffered conditions results in the formation of additional magnetite, whereas the bulk Fe^{3+}/Fe^{tot} ratio remains constant. As a consequence, the lizardite to antigorite phase transformation in a buffered system is not likely to affect the bulk redox budget. The observed decrease in both magnetite content and redox budget in natural serpentinites from lizardite-bearing to antigorite-bearing serpentinites thus likely reflects open-system behaviour and lack of a $f(O_2)$ buffer assemblage. In such an open system, the bulk Fe^{3+}/Fe^{tot} ratio further decreases to near zero during antigorite dehydration. Conversely, in a closed system where the bulk Fe^{3+}/Fe^{tot} ratio remains constant, the $f(O_2)$ will increase during antigorite dehydration and can lead to the formation of hematite.

We also document that the Fe^{3+}/Fe^{tot} ratio of both lizardite and antigorite strongly depends on the bulk Al_2O_3 concentration when serpentine is the sole host of Al. In this case, the Fe^{3+} concentration of serpentine is invariantly fixed by its Al content and independent of temperature.

In a closed system, during subduction metamorphism, the $f(O_2)$ is dictated by the constant bulk Fe^{3+}/Fe^{tot} ratio of the serpentinite assemblage. However, temperature-dependent partitioning of Al between serpentine and chlorite will influence the serpentine Fe^{3+}/Fe^{tot} ratio, making it effectively variable during subduction metamorphism. For most serpentinites, the $f(O_2)$ will be constrained between the FMQ-1 and HM (FMQ+3) buffers. These results confirm earlier calculations (Evans & Frost, 2021) and imply that the $f(O_2)$ of most serpentinites will remain below levels where significant oxidised sulphur species will be present in the fluids released by serpentinite dehydration. However, uncertainties in such fluid speciation calculations are largely unconstrained.

ACKNOWLEDGEMENTS

The authors thank Elias Kempf for the antigorite serpentinite sample, Raphael Njul and Alex Rother for sample preparation and Detlef Krauße for assistance with EPMA analysis. We further thank Johannes C. Vrijmoed and José Alberto Padrón-Navarta for discussion on the Gibbs energy minimisation and subduction

zone evolution. Carla Tiraboschi and an anonymous reviewer helped to improve the manuscript. Further thanks go to Carl Spandler for excellent editorial handling. This study was financed by the international research and training group Deep Earth Volatile Cycles DFG grant no. GRK 2156/1 and partly supported by the DFG grant FR 1555/11 and the NWO grant VI.Vidi.193.030.

DATA AVAILABILITY STATEMENT

The data underlying this article are available in the article and in its online supporting information.

SUPPLEMENTARY DATA

Supplementary data are available at Journal of Petrology online.

References

Alt, J. C., Schwarzenbach, E. M., Früh-Green, G. L., Shanks, W. C., III, Bernasconi, S. M., Garrido, C. J., Crispini, L., Gaggero, L., Padrón-Navarta, J. A. & Marchesi, C. (2013). The role of serpentinites in cycling of carbon and sulfur: seafloor serpentinization and subduction metamorphism. *Lithos* **178**, 40–54. https://doi.org/10.1016/j.lithos.2012.12.006.

Alt, J. C., Shanks, W. C., Crispini, L., Gaggero, L., Schwarzenbach, E. M., Früh-Green, G. L. & Bernasconi, S. M. (2012). Uptake of carbon and sulfur during seafloor serpentinization and the effects of subduction metamorphism in Ligurian peridotites. *Chemical Geology* **322-323**, 268–277. https://doi.org/10.1016/j.chemgeo.2012.07.009.

Arnulf, A. F., Bassett, D., Harding, A. J., Kodaira, S., Nakanishi, A. & Moore, G. (2022). Upper-plate controls on subduction zone geometry, hydration and earthquake behaviour. *Nature Geoscience* **15**, 143–148. https://doi.org/10.1038/s41561-021-00879-x.

Brigatti, M. F., Galli, E., Medici, L. & Poppi, L. (1997). Crystal structure refinement of aluminian lizardite-2H2. *American Mineralogist* **82**, 931–935. https://doi.org/10.2138/am-1997-9-1010.

Bromiley, G. D. & Pawley, A. R. (2003). The stability of antigorite in the system MgO-SiO2-H2O (MSH) and MgO-Al2O3-SiO2-H2O (MASH): the effects of Al3+ substitution on high-pressure stability. *American Mineralogist* **88**, 99–108. https://doi.org/10.2138/am-2003-0113.

Brounce, M., Cottrell, E. & Kelley, K. A. (2019). The redox budget of the Mariana subduction zone. *Earth and Planetary Science Letters* **528**, 115859. https://doi.org/10.1016/j.epsl.2019.115859.

Caciagli, N. C. & Manning, C. E. (2003). The solubility of calcite in water at 6-16 kbar and 500-800 °C. *Contributions to Mineralogy and Petrology* **146**, 275–285. https://doi.org/10.1007/s00410-003-0501-y.

Cannaò, E., Scambelluri, M., Agostini, S., Tonarini, S. & Godard, M. (2016). Linking serpentinite geochemistry with tectonic evolution at the subduction plate-interface: the Voltri massif case study (Ligurian Western Alps, Italy). *Geochimica et Cosmochimica Acta* **190**, 115–133. https://doi.org/10.1016/j.gca.2016.06.034.

Capitani, G. & Mellini, M. (2004). The modulated crystal structure of antigorite: the m = 17 polysome. *American Mineralogist* **89**, 147–158. https://doi.org/10.2138/am-2004-0117.

Chollet, M., Daniel, I., Koga, K. T., Morard, G. & van de Moortle, B. (2011). Kinetics and mechanism of antigorite dehydration: implications for subduction zone seismicity. *Journal of Geophysical Research: Solid Earth* **116**, 1–9. https://doi.org/10.1029/2010JB007739.

Connolly, J. A. D. (2005). Computation of phase equilibria by linear programming: a tool for geodynamic modeling and its application to subduction zone decarbonation. *Earth and Planetary Science Letters* **236**, 524–541. https://doi.org/10.1016/j.epsl.2005.04.033.

Debret, B., Andreani, M., Muñoz, M., Bolfan-Casanova, N., Carlut, J., Nicollet, C., Schwartz, S. & Trcera, N. (2014). Evolution of Fe redox state in serpentine during subduction. *Earth and Planetary Science Letters* **400**, 206–218. https://doi.org/10.1016/j.epsl.2014.05.038.

Debret, B., Bolfan-Casanova, N., Padrón-Navarta, J. A., Martin-Hernandez, F., Andreani, M., Garrido, C. J., López Sánchez-Vizcaíno, V., Gómez-Pugnaire, M. T., Muñoz, M. & Trcera, N. (2015). Redox state of iron during high-pressure serpentinite dehydration. *Contributions to Mineralogy and Petrology* **169**, 1–18. https://doi.org/10.1007/s00410-015-1130-y.

Debret, B. & Sverjensky, D. A. (2017). Highly oxidising fluids generated during serpentinite breakdown in subduction zones. *Scientific Reports* **7**, 10351–10356. https://doi.org/10.1038/s41598-017-09626-y.

Diener, J. F. A., Powell, R., White, R. W. & Holland, T. J. B. (2007). A new thermodynamic model for clino- and orthoamphiboles in the system Na2O-CaO-FeO-MgO-Al2O3-SiO2-H2O-O. *Journal of Metamorphic Geology* **25**, 631–656. https://doi.org/10.1111/j.1525-1314.2007.00720.x.

Eberhard, L., Plümper, O. & Frost, D. J. (2023). Early release of H2O during subduction of carbonated ultramafic lithologies. *Contributions to Mineralogy and Petrology* **178**, 17. https://doi.org/10.1007/s00410-023-01997-y.

Evans, B. W. (2004). The serpentinite multisystem revisited: chrysotile is metastable. *International Geology Review* **46**, 479–506. https://doi.org/10.2747/0020-6814.46.6.479.

Evans, B. W. (2008). Control of the products of serpentinization by the Fe2+ Mg-1 exchange potential of olivine and orthopyroxene. *Journal of Petrology* **49**, 1873–1887. https://doi.org/10.1093/petrology/egn050.

Evans, B. W., Dyar, D. M. & Kuehner, S. M. (2012). Implications of ferrous and ferric iron in antigorite. *American Mineralogist* **97**, 184–196. https://doi.org/10.2138/am.2012.3926.

Evans, K. A. & Frost, B. R. (2021). Deserpentinization in subduction zones as a source of oxidation in arcs: a reality check. *Journal of Petrology* **62**, 1–32. https://doi.org/10.1093/petrology/egab016.

Evans, K. A. & Powell, R. (2015). The effect of subduction on the sulphur, carbon and redox budget of lithospheric mantle. *Journal of Metamorphic Geology* **33**, 649–670. https://doi.org/10.1111/jmg.12140.

Evans, K. A., Reddy, S. M., Tomkins, A. G., Crossley, R. J. & Frost, B. R. (2017). Effects of geodynamic setting on the redox state of fluids released by subducted mantle lithosphere. *Lithos* **278-281**, 26–42. https://doi.org/10.1016/j.lithos.2016.12.023.

Flemetakis, S., Tiraboschi, C., Rohrbach, A., Berndt, J. & Klemme, S. (2022). The stability of antigorite in subduction zones revisited: the effect of F on antigorite stability and its breakdown reactions at high pressures and high temperatures, with implications for the geochemical cycles of halogens. *Contributions to Mineralogy and Petrology* **177**, 70. https://doi.org/10.1007/s00410-022-01934-5.

Frost, R. B. (1985). On the stability of sulfides, oxides, and native metals in serpentinite. *Journal of Petrology* **26**, 31–63. https://doi.org/10.1093/petrology/26.1.31.

Frost, R. B. & Beard, J. S. (2007). On silica activity and serpentinization. *Journal of Petrology* **48**, 1351–1368. https://doi.org/10.1093/petrology/egm021.

Hatakeyama, K., Katayama, I., Hirauchi, K. I. & Michibayashi, K. (2017). Mantle hydration along outer-rise faults inferred from

serpentinite permeability. *Scientific Reports* **7**, 13870. https://doi.org/10.1038/s41598-017-14309-9.

Hilairet, N., Daniel, I. & Reynard, B. (2006). Equation of state of antigorite, stability field of serpentines, and seismicity in subduction zones. *Geophysical Research Letters* **33**, 1–4. https://doi.org/10.1029/2005GL024728.

Holland, T. J. B. & Powell, R. (2011). An improved and extended internally consistent thermodynamic dataset for phases of petrological interest, involving a new equation of state for solids. *Journal of Metamorphic Geology* **29**, 333–383. https://doi.org/10.1111/j.1525-1314.2010.00923.x.

Huber, K., Vrijmoed, J. C. & John, T. (2022). Formation of olivine veins by reactive fluid flow in a dehydrating serpentinite. *Geochemistry, Geophysics, Geosystems* **23**. https://doi.org/10.1029/2021GC010267.

Iacovino, K., Guild, M. R. & Till, C. B. (2020). Aqueous fluids are effective oxidizing agents of the mantle in subduction zones. *Contributions to Mineralogy and Petrology* **175**, 36. https://doi.org/10.1007/s00410-020-1673-4.

Jennings, E. S. & Holland, T. J. B. (2015). A simple thermodynamic model for melting of peridotite in the system NCFMASOCr. *Journal of Petrology* **56**, 869–892. https://doi.org/10.1093/petrology/egv020.

Kelley, K. A. & Cottrell, E. (2009). Water and the oxidation state of subduction zone magmas. *Science* **325**, 605–607. https://doi.org/10.1126/science.1174156.

Keppler, H. & Frost, D. J. (2005). Introduction to minerals under extreme conditions. *Mineral Behaviour at Extreme Conditions* **6**, 1–30. https://doi.org/10.1180/EMU-notes.7.1.

Klein, F., Bach, W., Humphris, S. E., Kahl, W., Jöns, N., Moskowitz, B. & Berquó, T. S. (2014). Magnetite in seafloor serpentinite—some like it hot. *Geology* **42**, 135–138. https://doi.org/10.1130/G35068.1.

Li, X. P., Rahn, M. & Bucher, K. (2004). Serpentinites of the Zermatt-Saas ophiolite complex and their texture evolution. *Journal of Metamorphic Geology* **22**, 159–177. https://doi.org/10.1111/j.1525-1314.2004.00503.x.

Manning, C. E. (2013). Thermodynamic modeling of fluid-rock interaction at mid-crustal to upper-mantle conditions. *Reviews in Mineralogy and Geochemistry* **76**, 135–164. https://doi.org/10.2138/rmg.2013.76.5.

Maurice, J., Bolfan-Casanova, N., Demouchy, S., Chauvigne, P., Schiavi, F. & Debret, B. (2020). The intrinsic nature of antigorite breakdown at 3 GPa: experimental constraints on redox conditions of serpentinite dehydration in subduction zones. *Contributions to Mineralogy and Petrology* **175**, 94. https://doi.org/10.1007/s00410-020-01731-y.

Mayhew, L. E. & Ellison, E. T. (2020). A synthesis and meta-analysis of the Fe chemistry of serpentinites and serpentine minerals. *Philosophical Transactions of the Royal Society A: Mathematical, Physical and Engineering Sciences* **378**, 20180420. https://doi.org/10.1098/rsta.2018.0420.

McCollom, T. M., Klein, F., Moskowitz, B., Berquó, T. S., Bach, W. & Templeton, A. S. (2020a). Hydrogen generation and iron partitioning during experimental serpentinization of an olivine–pyroxene mixture. *Geochimica et Cosmochimica Acta* **282**, 55–75. https://doi.org/10.1016/j.gca.2020.05.016.

McCollom, T. M., Klein, F., Solheid, P. & Moskowitz, B. (2020b). The effect of pH on rates of reaction and hydrogen generation during serpentinization. *Philosophical Transactions of the Royal Society A: Mathematical, Physical and Engineering Sciences* **378**, 20180428. https://doi.org/10.1098/rsta.2018.0428.

Mellini, M. (1982). The crystal structure of lizardite 1T: hydrogen bonds and polytypism. *American Mineralogist* **67**, 587–598.

Mellini, M., Trommsdorff, V. & Compagnoni, R. (1987). Antigorite polysomatism: behaviour during progressive metamorphism. *Contributions to Mineralogy and Petrology* **97**, 147–155. https://doi.org/10.1007/BF00371235.

Mellini, M. & Zanazzi, P. F. (1987). Crystal structures of lizardite_1T and lizardite-2H1 from coli, Italy. *American Mineralogist* **72**, 943–948.

Merkulova, M., Muñoz, M., Vidal, O. & Brunet, F. (2016). Role of iron content on serpentinite dehydration depth in subduction zones: experiments and thermodynamic modeling. *Lithos* **264**, 441–452. https://doi.org/10.1016/j.lithos.2016.09.007.

Merkulova, M. V., Muñoz, M., Brunet, F., Vidal, O., Hattori, K., Vantelon, D., Trcera, N. & Huthwelker, T. (2017). Experimental insight into redox transfer by iron- and sulfur-bearing serpentinite dehydration in subduction zones. *Earth and Planetary Science Letters* **479**, 133–143. https://doi.org/10.1016/j.epsl.2017.09.009.

Padrón-Navarta, J. A., Hermann, J., Garrido, C. J., López Sánchez-Vizcaíno, V. & Gómez-Pugnaire, M. T. (2010). An experimental investigation of antigorite dehydration in natural silica-enriched serpentinite. *Contributions to Mineralogy and Petrology* **159**, 25–42. https://doi.org/10.1007/s00410-009-0414-5.

Padrón-Navarta, J. A., Lopez Sanchez-Vizcaino, V., Garrido, C. J. & Gomez-Pugnaire, M. T. (2011). Metamorphic record of high-pressure dehydration of antigorite Serpentinite to chlorite Harzburgite in a subduction setting (Cerro del Almirez, Nevado-Filabride Complex, Southern Spain). *Journal of Petrology* **52**, 2047–2078. https://doi.org/10.1093/petrology/egr039.

Padrón-Navarta, J. A., López Sánchez-Vizcaíno, V., Menzel, M. D., Gómez-Pugnaire, M. T. & Garrido, C. J. (2023). Mantle wedge oxidation from deserpentinization modulated by sediment-derived fluids. *Nature Geoscience* **16**, 268–275. https://doi.org/10.1038/s41561-023-01127-0.

Padrón-Navarta, J. A., Sánchez-Vizcaíno, V. L., Hermann, J., Connolly, J. A. D., Garrido, C. J., Gómez-Pugnaire, M. T. & Marchesi, C. (2013). Tschermak's substitution in antigorite and consequences for phase relations and water liberation in high-grade serpentinites. *Lithos* **178**, 186–196. https://doi.org/10.1016/j.lithos.2013.02.001.

Parkinson, I. J. & Arculus, R. J. (1999). The redox state of subduction zones: insights from arc-peridotites. *Chemical Geology* **160**, 409–423. https://doi.org/10.1016/S0009-2541(99)00110-2.

Peacock, S. M. (1990). Fluid processes in subduction zones. *Science* **248**, 329–337. https://doi.org/10.1126/science.248.4953.329.

Peretti, A., Dubessy, J., Mullis, J., Ronald Frost, B. & Trommsdorff, V. (1992). Highly reducing conditions during Alpine metamorphism of the Malenco peridotite (Sondrio, northern Italy) indicated by mineral paragenesis and H2 in fluid inclusions. *Contributions to Mineralogy and Petrology* **112**, 329–340. https://doi.org/10.1007/BF00310464.

Perrillat, J.-P., Daniel, I., Koga, K. T., Reynard, B., Cardon, H. & Crichton, W. A. (2005). Kinetics of antigorite dehydration: a real-time X-ray diffraction study. *Earth and Planetary Science Letters* **236**, 899–913. https://doi.org/10.1016/j.epsl.2005.06.006.

Piccoli, F., Hermann, J., Pettke, T., Connolly, J. A. D., Kempf, E. D. & Vieira Duarte, J. F. (2019). Subducting serpentinites release reduced, not oxidized, aqueous fluids. *Scientific Reports* **9**, 19573. https://doi.org/10.1038/s41598-019-55944-8.

Pitzer, K. S. & Sterner, S. M. (1994). Equations of state valid continuously from zero to extreme pressures for H2O and CO2. *Journal of Chemical Physics* **101**, 3111–3116. https://doi.org/10.1063/1.467624.

Plümper, O., John, T., Podladchikov, Y. Y., Vrijmoed, J. C. & Scambelluri, M. (2017). Fluid escape from subduction zones controlled by channel-forming reactive porosity. *Nature Geoscience* **10**, 150–156. https://doi.org/10.1038/ngeo2865.

Prescher, C., McCammon, C. & Dubrovinsky, L. (2012). MossA: a program for analyzing energy-domain Mössbauer spectra from

conventional and synchrotron sources. *Journal of Applied Crystallography* **45**, 329–331. https://doi.org/10.1107/S0021889812004979.

Principi, G., Bortolotti, V., Chiari, M., Cortesogno, L., Gaggero, L., Marcucci, M., Saccani, E. & Treves, B. (2004). The pre-orogenic volcanosedimentary covers of the Western Tethys Oceanic basin: a review. *Ofioliti* **29**, 177–211.

Reynard, B., Fellah, C. & McCammon, C. (2022). Iron oxidation state in serpentines and magnesian chlorites of subduction-related rocks. *European Journal of Mineralogy* **34**, 645–656. https://doi.org/10.5194/ejm-34-645-2022.

Rüpke, L. H., Morgan, J. P., Hort, M. & Connolly, J. A. D. (2004). Serpentine and the subduction zone water cycle. *Earth and Planetary Science Letters* **223**, 17–34. https://doi.org/10.1016/j.epsl.2004.04.018.

Scambelluri, M., Cannaò, E. & Gilio, M. (2019). The water and fluid-mobile element cycles during serpentinite subduction. A review. *European Journal of Mineralogy* **31**, 405–428. https://doi.org/10.1127/ejm/2019/0031-2842.

Schwartz, S., Guillot, S., Reynard, B., Lafay, R., Debret, B., Nicollet, C., Lanari, P. & Auzende, A. L. (2013). Pressure-temperature estimates of the lizardite/antigorite transition in high pressure serpentinites. *Lithos* **178**, 197–210. https://doi.org/10.1016/j.lithos.2012.11.023.

Spandler, C. & Pirard, C. (2013). Element recycling from subducting slabs to arc crust: a review. *Lithos* **170-171**, 208–223. https://doi.org/10.1016/j.lithos.2013.02.016.

Stagno, V., Frost, D. J., McCammon, C. A., Mohseni, H. & Fei, Y. (2015). The oxygen fugacity at which graphite or diamond forms from carbonate-bearing melts in eclogitic rocks. *Contributions to Mineralogy and Petrology* **169**. https://doi.org/10.1007/s00410-015-1111-1.

Syracuse, E. M., van Keken, P. E. & Abers, G. A. (2010). The global range of subduction zone thermal models. *Physics of the Earth and Planetary Interiors* **183**, 73–90. https://doi.org/10.1016/j.pepi.2010.02.004.

Tajčmanová, L., Connolly, J. A. D. & Cesare, B. (2009). A thermodynamic model for titanium and ferric iron solution in biotite. *Journal of Metamorphic Geology* **27**, 153–165. https://doi.org/10.1111/j.1525-1314.2009.00812.x.

Tiraboschi, C., McCammon, C., Rohrbach, A., Klemme, S., Berndt, J. & Sanchez-Valle, C. (2023). Preferential mobilisation of oxidised iron by slab-derived hydrous silicate melts. *Geochemical Perspectives Letters* **24**, 43–47. https://doi.org/10.7185/geochemlet.2304.

Ulmer, P. & Trommsdorff, V. (1995). Serpentine stability to mantle depths and subduction-related magmatism. *Science* **268**, 858–861. https://doi.org/10.1126/science.268.5212.858.

Vitale Brovarone, A., Martinez, I., Elmaleh, A., Compagnoni, R., Chaduteau, C., Ferraris, C. & Esteve, I. (2017). Massive production of abiotic methane during subduction evidenced in metamorphosed ophicarbonates from the Italian Alps. *Nature Communications* **8**, 14134. https://doi.org/10.1038/ncomms14134.

von Seckendorff, V., O'Neill, H. S. & C. (1993). An experimental study on Fe-Mg partitioning between olivine and orthopyroxene at 1173, 1273 and 1473 K and 1.6 GPa. *Contributions to Mineralogy and Petrology* **113**, 196–207. https://doi.org/10.1007/BF00283228.

Walters, J. B., Cruz-Uribe, A. M. & Marshall, H. R. (2020). Sulfur loss from subducted altered oceanic crust and implications for mantle oxidation. *Geochemical Perspective Letters* **13**, 36–41. https://doi.org/10.7185/geochemlet.2011.

White, R. W., Powell, R., Holland, T. J. B., Johnson, T. E. & Green, E. C. R. (2014). New mineral activity-composition relations for thermodynamic calculations in metapelitic systems. *Journal of Metamorphic Geology* **32**, 261–286. https://doi.org/10.1111/jmg.12071.

Whitney, D. L. & Evans, B. W. (2010). Abbreviations for names of rock-forming minerals. *American Mineralogist* **95**, 185–187. https://doi.org/10.2138/am.2010.3371.

Woodland, A. B. & O'Neill, H. S. C. (1997). Thermodynamic data for Fe-bearing phases obtained using noble metal alloys as redox sensors. *Geochimica et Cosmochimica Acta* **61**, 4359–4366. https://doi.org/10.1016/S0016-7037(97)00247-0.

Wunder, B., Baronnet, A. & Schreyer, W. (1997). Ab-initio synthesis and TEM confirmation of antigorite in the system MgO-SiO2-H2O. *American Mineralogist* **82**, 760–764. https://doi.org/10.2138/am-1997-7-814.

Wunder, B. & Schreyer, W. (1997). Antigorite: high-pressure stability in the system MgO-SiO_2-H_2O (MSH). *Lithos* **41**, 213–227. https://doi.org/10.1016/S0024-4937(97)82013-0.

Wunder, B., Wirth, R. & Gottschalk, M. (2001). Antigorite: pressure and temperature dependence of polysomatism and water content. *European Journal of Mineralogy* **13**, 485–495. https://doi.org/10.1127/0935-1221/2001/0013-0485.